The Astrophysical Journal, 720:435–453, 2010 September 1 doi:10.1088/0004-637X/720/1/435

THE *FERMI*-LAT HIGH-LATITUDE SURVEY: SOURCE COUNT DISTRIBUTIONS AND THE ORIGIN OF THE EXTRAGALACTIC DIFFUSE BACKGROUND

A. A. Abdo[1,2], M. Ackermann[3,52], M. Ajello[3,52], E. Antolini[4,5], L. Baldini[6], J. Ballet[7], G. Barbiellini[8,9], D. Bastieri[10,11], B. M. Baughman[12], K. Bechtol[3,52], R. Bellazzini[6], B. Berenji[3,52], R. D. Blandford[3,52], E. D. Bloom[3,52], E. Bonamente[4,5], A. W. Borgland[3,52], A. Bouvier[3,52], J. Bregeon[6], A. Brez[6], M. Brigida[13,14], P. Bruel[15], T. H. Burnett[16], S. Buson[10], G. A. Caliandro[17], R. A. Cameron[3,52], P. A. Caraveo[18], S. Carrigan[11], J. M. Casandjian[7], E. Cavazzuti[19], C. Cecchi[4,5], Ö. Çelik[20,21,22], E. Charles[3,52], A. Chekhtman[1,23], C. C. Cheung[1,2], J. Chiang[3,52], S. Ciprini[5], R. Claus[3,52], J. Cohen-Tanugi[24], J. Conrad[25,26,53], L. Costamante[3,52], S. Cutini[19], C. D. Dermer[1], A. de Angelis[27], F. de Palma[13,14], E. do Couto e Silva[3,52], P. S. Drell[3,52], R. Dubois[3,52], D. Dumora[28,29], C. Farnier[24], C. Favuzzi[13,14], S. J. Fegan[15], W. B. Focke[3,52], Y. Fukazawa[30], S. Funk[3,52], P. Fusco[13,14], F. Gargano[14], D. Gasparrini[19], N. Gehrels[20], S. Germani[4,5], N. Giglietto[13,14], P. Giommi[19], F. Giordano[13,14], T. Glanzman[3,52], G. Godfrey[3,52], I. A. Grenier[7], J. E. Grove[1], S. Guiriec[31], D. Hadasch[32], M. Hayashida[3,52], E. Hays[20], S. E. Healey[3,52], D. Horan[15], R. E. Hughes[12], R. Itoh[30], G. Jóhannesson[3,52], A. S. Johnson[3,52], T. J. Johnson[20,33], W. N. Johnson[1], T. Kamae[3,52], H. Katagiri[30], J. Kataoka[34], N. Kawai[35,36], J. Knödlseder[37], M. Kuss[6], J. Lande[3,52], L. Latronico[6], S.-H. Lee[3,52], M. Lemoine-Goumard[28,29], M. Llena Garde[25,26], F. Longo[8,9], F. Loparco[13,14], B. Lott[28,29], M. N. Lovellette[1], P. Lubrano[4,5], G. M. Madejski[3,52], A. Makeev[1,23], M. N. Mazziotta[14], W. McConville[20,33], J. E. McEnery[20,33], C. Meurer[25,26], P. F. Michelson[3,52], W. Mitthumsiri[3,52], T. Mizuno[30], C. Monte[13,14], M. E. Monzani[3,52], A. Morselli[38], I. V. Moskalenko[3,52], S. Murgia[3,52], P. L. Nolan[3,52], J. P. Norris[39], E. Nuss[24], T. Ohsugi[40], N. Omodei[3,52], E. Orlando[41], J. F. Ormes[39], M. Ozaki[42], D. Paneque[3,52], J. H. Panetta[3,52], D. Parent[1,23,28,29], V. Pelassa[24], M. Pepe[4,5], M. Pesce-Rollins[6], F. Piron[24], T. A. Porter[3,52], S. Rainò[13,14], R. Rando[10,11], M. Razzano[6], A. Reimer[3,43,52], O. Reimer[3,43,52], S. Ritz[44], L. S. Rochester[3,52], A. Y. Rodriguez[17], R. W. Romani[3,52], M. Roth[16], H. F.-W. Sadrozinski[44], A. Sander[12], P. M. Saz Parkinson[44], J. D. Scargle[45], C. Sgrò[6], M. S. Shaw[3,52], P. D. Smith[12], G. Spandre[6], P. Spinelli[13,14], J.-L. Starck[7], M. S. Strickman[1], A. W. Strong[41], D. J. Suson[46], H. Tajima[3,52], H. Takahashi[40], T. Takahashi[42], T. Tanaka[3,52], J. B. Thayer[3,52], J. G. Thayer[3,52], D. J. Thompson[20], L. Tibaldo[7,10,11,54], D. F. Torres[32,17], G. Tosti[4,5], A. Tramacere[3,47,48,52], Y. Uchiyama[3,52], T. L. Usher[3,52], V. Vasileiou[21,22], N. Vilchez[37], V. Vitale[38,49], A. P. Waite[3,52], P. Wang[3,52], B. L. Winer[12], K. S. Wood[1], Z. Yang[25,26], T. Ylinen[26,50,51], and M. Ziegler[44]

[1] Space Science Division, Naval Research Laboratory, Washington, DC 20375, USA
[2] National Academy of Sciences, Washington, DC 20001, USA
[3] W. W. Hansen Experimental Physics Laboratory, Kavli Institute for Particle Astrophysics and Cosmology, Department of Physics and SLAC National Accelerator Laboratory, Stanford University, Stanford, CA 94305, USA; majello@slac.stanford.edu, tramacer@slac.stanford.edu
[4] Istituto Nazionale di Fisica Nucleare, Sezione di Perugia, I-06123 Perugia, Italy
[5] Dipartimento di Fisica, Università degli Studi di Perugia, I-06123 Perugia, Italy
[6] Istituto Nazionale di Fisica Nucleare, Sezione di Pisa, I-56127 Pisa, Italy
[7] Laboratoire AIM, CEA-IRFU/CNRS/Université Paris Diderot, Service d'Astrophysique, CEA Saclay, 91191 Gif sur Yvette, France
[8] Istituto Nazionale di Fisica Nucleare, Sezione di Trieste, I-34127 Trieste, Italy
[9] Dipartimento di Fisica, Università di Trieste, I-34127 Trieste, Italy
[10] Istituto Nazionale di Fisica Nucleare, Sezione di Padova, I-35131 Padova, Italy
[11] Dipartimento di Fisica "G. Galilei," Università di Padova, I-35131 Padova, Italy
[12] Department of Physics, Center for Cosmology and Astro-Particle Physics, The Ohio State University, Columbus, OH 43210, USA
[13] Dipartimento di Fisica "M. Merlin" dell'Università e del Politecnico di Bari, I-70126 Bari, Italy
[14] Istituto Nazionale di Fisica Nucleare, Sezione di Bari, 70126 Bari, Italy
[15] Laboratoire Leprince-Ringuet, École polytechnique, CNRS/IN2P3, Palaiseau, France
[16] Department of Physics, University of Washington, Seattle, WA 98195-1560, USA
[17] Institut de Ciencies de l'Espai (IEEC-CSIC), Campus UAB, 08193 Barcelona, Spain
[18] INAF-Istituto di Astrofisica Spaziale e Fisica Cosmica, I-20133 Milano, Italy
[19] Agenzia Spaziale Italiana (ASI) Science Data Center, I-00044 Frascati (Roma), Italy
[20] NASA Goddard Space Flight Center, Greenbelt, MD 20771, USA
[21] Center for Research and Exploration in Space Science and Technology (CRESST) and NASA Goddard Space Flight Center, Greenbelt, MD 20771, USA
[22] Department of Physics and Center for Space Sciences and Technology, University of Maryland Baltimore County, Baltimore, MD 21250, USA
[23] George Mason University, Fairfax, VA 22030, USA
[24] Laboratoire de Physique Théorique et Astroparticules, Université Montpellier 2, CNRS/IN2P3, Montpellier, France
[25] Department of Physics, Stockholm University, AlbaNova, SE-106 91 Stockholm, Sweden
[26] The Oskar Klein Centre for Cosmoparticle Physics, AlbaNova, SE-106 91 Stockholm, Sweden
[27] Dipartimento di Fisica, Università di Udine and Istituto Nazionale di Fisica Nucleare, Sezione di Trieste, Gruppo Collegato di Udine, I-33100 Udine, Italy
[28] CNRS/IN2P3, Centre d'Études Nucléaires Bordeaux Gradignan, UMR 5797, Gradignan, 33175, France
[29] Université de Bordeaux, Centre d'Études Nucléaires Bordeaux Gradignan, UMR 5797, Gradignan, 33175, France
[30] Department of Physical Sciences, Hiroshima University, Higashi-Hiroshima, Hiroshima 739-8526, Japan
[31] Center for Space Plasma and Aeronomic Research (CSPAR), University of Alabama in Huntsville, Huntsville, AL 35899, USA
[32] Institució Catalana de Recerca i Estudis Avançats (ICREA), Barcelona, Spain
[33] Department of Physics and Department of Astronomy, University of Maryland, College Park, MD 20742, USA
[34] Research Institute for Science and Engineering, Waseda University, 3-4-1, Okubo, Shinjuku, Tokyo 169-8555, Japan
[35] Department of Physics, Tokyo Institute of Technology, Meguro City, Tokyo 152-8551, Japan
[36] Cosmic Radiation Laboratory, Institute of Physical and Chemical Research (RIKEN), Wako, Saitama 351-0198, Japan
[37] Centre d'Étude Spatiale des Rayonnements, CNRS/UPS, BP 44346, F-30128 Toulouse Cedex 4, France
[38] Istituto Nazionale di Fisica Nucleare, Sezione di Roma "Tor Vergata," I-00133 Roma, Italy

[39] Department of Physics and Astronomy, University of Denver, Denver, CO 80208, USA
[40] Hiroshima Astrophysical Science Center, Hiroshima University, Higashi-Hiroshima, Hiroshima 739-8526, Japan
[41] Max-Planck Institut für extraterrestrische Physik, 85748 Garching, Germany
[42] Institute of Space and Astronautical Science, JAXA, 3-1-1 Yoshinodai, Sagamihara, Kanagawa 229-8510, Japan
[43] Institut für Astro- und Teilchenphysik and Institut für Theoretische Physik, Leopold-Franzens-Universität Innsbruck, A-6020 Innsbruck, Austria
[44] Santa Cruz Institute for Particle Physics, Department of Physics and Department of Astronomy and Astrophysics, University of California at Santa Cruz, Santa Cruz, CA 95064, USA
[45] Space Sciences Division, NASA Ames Research Center, Moffett Field, CA 94035-1000, USA
[46] Department of Chemistry and Physics, Purdue University Calumet, Hammond, IN 46323-2094, USA
[47] Consorzio Interuniversitario per la Fisica Spaziale (CIFS), I-10133 Torino, Italy
[48] INTEGRAL Science Data Centre, CH-1290 Versoix, Switzerland
[49] Dipartimento di Fisica, Università di Roma "Tor Vergata," I-00133 Roma, Italy
[50] Department of Physics, Royal Institute of Technology (KTH), AlbaNova, SE-106 91 Stockholm, Sweden
[51] School of Pure and Applied Natural Sciences, University of Kalmar, SE-391 82 Kalmar, Sweden
Received 2010 February 11; accepted 2010 July 6; published 2010 August 11

ABSTRACT

This is the first of a series of papers aimed at characterizing the populations detected in the high-latitude sky of the *Fermi*-LAT survey. In this work, we focus on the intrinsic spectral and flux properties of the source sample. We show that when selection effects are properly taken into account, *Fermi* sources are on average steeper than previously found (e.g., in the bright source list) with an average photon index of 2.40 ± 0.02 over the entire 0.1–100 GeV energy band. We confirm that flat spectrum radio quasars have steeper spectra than BL Lacertae objects with an average index of 2.48 ± 0.02 versus 2.18 ± 0.02. Using several methods, we build the deepest source count distribution at GeV energies, deriving that the intrinsic source (i.e., blazar) surface density at $F_{100} \geqslant 10^{-9}$ ph cm^{-2} s^{-1} is $0.12^{+0.03}_{-0.02}$ deg^{-2}. The integration of the source count distribution yields that point sources contribute 16($\pm$1.8)% ($\pm$7% systematic uncertainty) of the GeV isotropic diffuse background. At the fluxes currently reached by LAT, we can rule out the hypothesis that pointlike sources (i.e., blazars) produce a larger fraction of the diffuse emission.

Key words: cosmology: observations – diffuse radiation – galaxies: active – galaxies: jets – gamma rays: diffuse background – surveys

Online-only material: color figures

1. INTRODUCTION

The origin of the extragalactic gamma-ray background (EGB) at GeV γ-rays is one of the fundamental unsolved problems in astrophysics. The EGB was first detected by the SAS-2 mission (Fichtel et al. 1975) and its spectrum was measured with good accuracy by the Energetic Gamma-Ray Experiment Telescope (EGRET; Sreekumar et al. 1998; Strong et al. 2004) on board the *Compton Observatory*. These observations by themselves do not provide much insight into the sources of the EGB.

Blazars, active galactic nuclei (AGNs) with a relativistic jet pointing close to our line of sight, represent the most numerous population detected by EGRET (Hartman et al. 1999) and their flux constitutes 15% of the total EGB intensity (resolved sources plus diffuse emission). Therefore, undetected blazars (e.g., all the blazars under the sensitivity level of EGRET) are the most likely candidates for the origin of the bulk of the EGB emission. Studies of the luminosity function of blazars showed that the contribution of blazars to the EGRET EGB could be in the range from 20% to 100% (e.g., Stecker & Salamon 1996; Chiang & Mukherjee 1998; Mücke & Pohl 2000), although the newest derivations suggest that blazars are responsible for only ~20%–40% of the EGB (e.g., Narumoto & Totani 2006; Dermer 2007; Inoue & Totani 2009).

It is thus possible that the EGB emission encrypts in itself the signature of some of the most powerful and interesting phenomena in astrophysics. Intergalactic shocks produced by the assembly of large-scale structures (e.g., Loeb & Waxman 2000; Miniati 2002; Keshet et al. 2003; Gabici & Blasi 2003), γ-ray emission from galaxy clusters (e.g., Berrington & Dermer 2003; Pfrommer et al. 2008), and emission from starburst as well as normal galaxies (e.g., Pavlidou & Fields 2002; Thompson et al. 2007) are among the most likely candidates for the generation of diffuse the GeV emission. Dark matter (DM), which constitutes more than 80% of the matter in the universe, can also provide a diffuse, cosmological, background of γ-rays. Indeed, supersymmetric theories with R-parity predict that the lightest DM particles (i.e., the neutralinos) are stable and can annihilate into GeV γ-rays (e.g., Jungman et al. 1996; Bergström 2000; Ullio et al. 2002; Ahn et al. 2007).

With the advent of the *Fermi* Large Area Telescope (LAT), a better understanding of the origin of the GeV diffuse emission becomes possible. *Fermi* has recently performed a new measurement of the EGB spectrum (also called isotropic diffuse background; Abdo et al. 2010d). This has been found to be consistent with a featureless power law with a photon index of ~2.4 in the 0.2–100 GeV energy range. The integrated flux ($E \geqslant 100$ MeV) of $1.03(\pm 0.17) \times 10^{-5}$ ph cm^{-2} s^{-1} sr^{-1} has been found to be significantly lower than the one of $1.45(\pm 0.05) \times 10^{-5}$ ph cm^{-2} s^{-1} sr^{-1} determined from EGRET data (see Sreekumar et al. 1998).

In this study, we address the contribution of *unresolved* point sources to the GeV diffuse emission and we discuss the implications. Early findings on the integrated emission of *unresolved* blazars were already reported in Abdo et al. (2009a) using a sample of bright AGNs detected in the first three months of *Fermi* observations. The present work represents a large

[52] National Research Council Research Associate.
[53] Royal Swedish Academy of Sciences Research Fellow, funded by a grant from the K. A. Wallenberg Foundation.
[54] Partially supported by the International Doctorate on Astroparticle Physics (IDAPP) program.

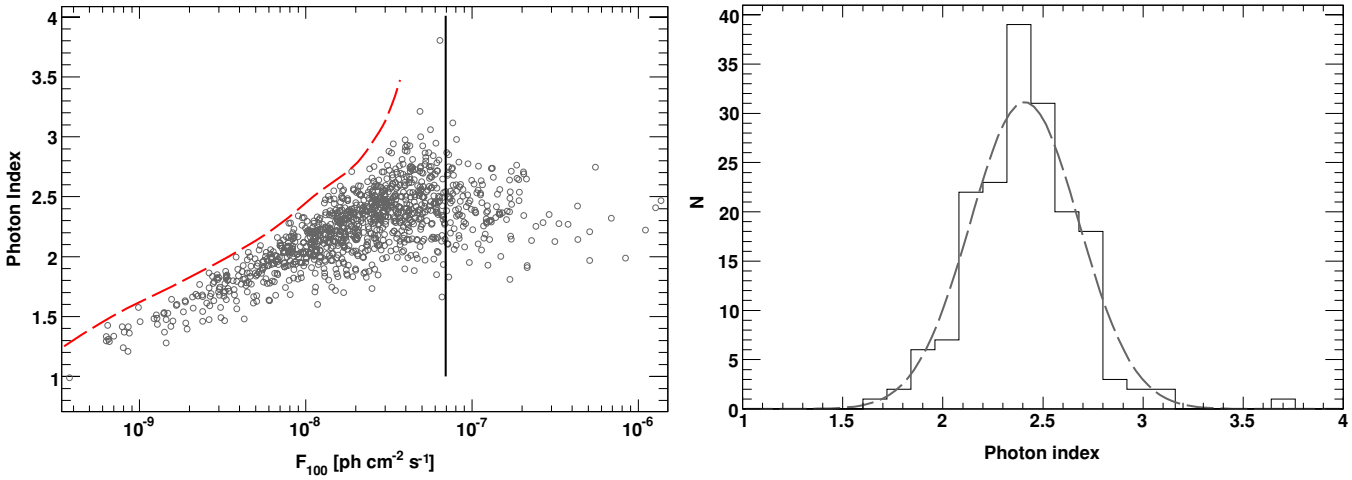

Figure 1. Left panel: flux–photon index plane for all the $|b| \geqslant 10^{\circ}$ sources with TS $\geqslant 25$. The dashed line is the flux limit as a function of photon index reported in Abdo et al. (2010e), while the solid line represents the limiting flux above which the spectral selection effects become negligible. Right panel: photon index distribution of all sources for $F_{100} \geqslant 7 \times 10^{-8}$ ph cm^{-2} s^{-1}. Above this limit, the LAT selection effect toward hard sources becomes negligible.
(A color version of this figure is available in the online journal.)

advance, with ∼4 times more blazars and a detailed investigation of selection effects in source detection.

This work is organized as follows. In Section 3, the intrinsic spectral properties of the *Fermi* sources are determined. In Section 4, the Monte Carlo simulations used for this analyses are outlined with the inherent systematic uncertainties (see Section 5). Finally, the source count distributions are derived in Section 6 and Section 7, while the contribution of point sources to the GeV diffuse background is determined in Section 8. Section 9 discusses and summarizes our findings. Since the final goal of this work is to derive the contribution of sources to the EGB, we will only use physical quantities (i.e., source flux and photon index) averaged over the time (11 months) included in the analysis for the First *Fermi*-LAT catalog (1FGL; Abdo et al. 2010b).

2. TERMINOLOGY

Throughout this paper, we use a few terms which might not be familiar to the reader. In this section, meanings of the most often used are clarified.

1. *Spectral bias (or photon-index bias).* It is the selection effect which allows *Fermi*-LAT to detect spectrally hard sources at fluxes generally fainter than those of soft sources.
2. *Flux-limited sample*. It refers to a sample which is uniformly selected solely according to the source flux. If the flux limit is chosen to be bright enough (as in the case of this paper), then the selection effects affecting any other properties (e.g., the source spectrum) of the sample are negligible. This is a truly uniformly selected sample.
3. *Diffuse emission from unresolved point sources*. It represents a measurement of the integrated emission from sources that have not been detected by *Fermi*. As it will be shown in the next sections, for each source detected at low fluxes, there is a large number of sources that have not been detected because of selection effects (e.g., the local background was too large or the photon index was too soft, or a combination of both). The diffuse emission from *unresolved* point sources (computed in this work) addresses the contribution of all of those sources that have not been detected because of these selection effects, but have a flux that is formally larger than the faintest *detected* source.

3. AVERAGE SPECTRAL PROPERTIES

3.1. Intrinsic Photon-index Distributions

As already shown in Abdo et al. (2009a; but see also Figure 1), at faint fluxes the LAT more easily detects hard-spectrum sources rather than sources with a soft spectrum. Sources with a photon index (e.g., the exponent of the power-law fit to the source photon spectrum) of 1.5 can be detected to fluxes that are a factor >20 fainter than those at which a source with a photon index of 3.0 can be detected (see Abdo et al. 2010e, for details). Thus, given this strong selection effect, the intrinsic photon-index distribution is necessarily different from the observed one. An approach to recovering the intrinsic photon-index distribution is obtained by studying the sample above $F_{100} \approx 7 \times 10^{-8}$ ph cm^{-2} s^{-1} and $|b| \geqslant 10^{\circ}$ (see the right panel of Figure 1). Indeed, above this flux limit, LAT detects all sources irrespective of their photon index, flux, or position in the high-latitude sky. Above this limit, LAT detects 135 sources. Their photon-index distribution, reported in Figure 1, is compatible with a Gaussian distribution with a mean of 2.40 $\pm$ 0.02 and a dispersion of 0.24 $\pm$ 0.02. These values differ from the mean of 2.23 $\pm$ 0.01 and the dispersion of 0.33 $\pm$ 0.01 derived using the entire $|b| \geqslant 10^{\circ}$ sample. Similarly, the intrinsic photon-index distributions of flat spectrum radio quasars (FSRQs) and BL Lacertae objects (BL Lac objects) are different from the observed distributions. In both cases, the *observed* average photon index is harder than the intrinsic average value. The results are summarized in Table 1.

3.2. Stacking Analysis

Another way to determine the average spectral properties is by stacking source spectra together. This is particularly simple since Abdo et al. (2010b) report the source flux in five different energy bands. We thus performed a stacking analysis of those sources with $F_{100} \geqslant 7 \times 10^{-8}$ ph cm^{-2} s^{-1}, TS $\geqslant 25$, and $|b| \geqslant 10^{\circ}$. For each energy band, the average flux is computed as the weighted average of all source fluxes in that band using the

Table 1
Observed Versus Intrinsic Photon Indices Distributions for the *Fermi*/LAT Source Classes

SAMPLE	Observed Distribution		Intrinsic Distribution	
	Mean	σ	Mean	σ
ALL	2.24 ± 0.01	0.31 ± 0.01	2.40 ± 0.02	0.24 ± 0.02
FSRQ	2.44 ± 0.01	0.21 ± 0.01	2.47 ± 0.02	0.19 ± 0.02
BL Lac object	2.05 ± 0.02	0.29 ± 0.01	2.20 ± 0.04	0.22 ± 0.03

inverse of the flux variance as a weight. The average spectrum is shown in Figure 2. A power-law model gives a satisfactory fit to the data (e.g., $\chi^2/\mathrm{dof} \approx 1$), yielding a photon index of 2.41 ± 0.07, in agreement with the results of the previous section.

We repeated the same exercise separately for sources identified as FSRQs and BL Lac objects in the *flux-limited* sample. Both classes have an average spectrum which is compatible with a single power law over the whole energy band. FSRQs are characterized by an index of 2.45 ± 0.03, while BL Lac objects have an average index of 2.23 ± 0.03. The fact that on average FSRQs are steeper than BL Lac objects is apparent when looking at the stacked spectra reported in Figure 3.

4. MONTE CARLO SIMULATIONS

In order to robustly estimate the LAT sky coverage, we performed detailed Monte Carlo simulations. The scheme of the simulation procedure is an improved version of what has already been applied in Abdo et al. (2009a). We performed 18 end-to-end simulations of the LAT sky which resemble as closely as possible the observed one. The tool *gtobssim*[55] has been used for this purpose. For each simulation, we modeled the Galactic and isotropic diffuse backgrounds using models (e.g., gll_iem_v02.fit) currently recommended by the LAT team.

An isotropic population of pointlike sources was added to each simulated observation. The coordinates of each source were randomly drawn in order to produce an isotropic distribution on the sky. Source fluxes were randomly drawn from a standard $\log N$–$\log S$ distribution with parameters similar to the one observed by LAT (see the next section). Even though the method we adopt to derive the survey sensitivity does not depend on the normalization or the slope of the input $\log N$–$\log S$, using the real distribution allows simulated observations to be produced that closely resemble the sky as observed with the LAT. The photon index of each source was also drawn from a Gaussian distribution with mean of 2.40 and 1σ width of 0.28. As noted in the previous section, this distribution represents well the intrinsic (not the observed one) distribution of photon indices. The adopted dispersion is slightly larger than what was found in the previous section and it is derived from the analysis of the entire sample (see Section 6.2). In this framework, we are neglecting any possible dependence of the photon-index distribution with flux. Also, we remark that the approach used here to derive the source count distribution depends very weakly on the assumptions (e.g., the $\log N$–$\log S$ used) made in the simulations.

More than 45,000 randomly distributed sources have been generated for each realization of the simulations. Detection follows (albeit in a simpler way) the scheme used in Abdo et al. (2010b). This scheme adopts three energy bands for source detection. The first band includes all *front*-converting[56] and *back*-converting photons with energies larger than 200 MeV and 400 MeV, respectively. The second band starts at 1 GeV for front photons and at 2 GeV for back photons. The high-energy band starts at 5 GeV for front photons and at 10 GeV for back photons. The choice of combining front and back events with different energies is motivated by the fact that front events have a better point-spread function (PSF) than back ones. The two PSFs are similar when the energy of back-converting photons is approximately twice as that of front-converting ones. The image pixel sizes change according to the energy band and are 0.°1, 0.°2, and 0.°3 for the low-, medium-, and high-energy bands, respectively. The final list of *candidate* sources is obtained starting with the detection at the highest energy band and adding all those sources which, being detected at lower energy, have a position not consistent with those detected at high energy. The detection step uses *pgwave* for determining the position of the excesses and *pointfit* for refining the source position. *Pgwave* (Ciprini et al. 2007) is a tool that uses several approaches (e.g., wavelets, thresholding, image denoising, and a sliding cell algorithm) to find source candidates, while *pointfit* (e.g., Burnett et al. 2009) employs a simplified binned likelihood algorithm to optimize the source position.

All of the source candidates found at this stage are then ingested to the Maximum Likelihood (ML) algorithm *gtlike* to determine the significance and the spectral parameters. In this step all sources' spectra are modeled as single power laws. On average, for each simulation, only ∼1000 sources are detected (out of the 45,000 simulated ones) above a TS[57] of 25 and this is found to be in good agreement with the real data.

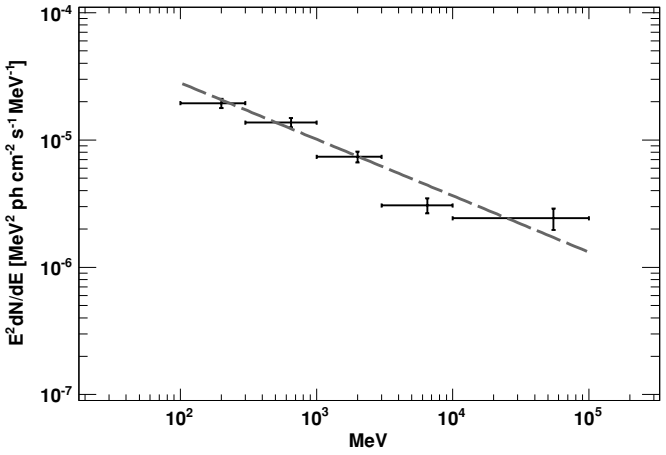

Figure 2. Stacked spectrum of sources in the *flux-limited* sample. The dashed line is the best power-law fit with a slope of 2.41 ± 0.07.

4.1. Performances of the Detection Algorithm on Real Data

In order to test the reliability of our detection pipeline, we applied it to the real one year data set. Our aim was to cross-check our result with the result reported in Abdo et al. (2010b). The flux above 100 MeV, computed from the power-law fit to the

[55] The list of science tools for the analysis of *Fermi* data is accessible at http://fermi.gsfc.nasa.gov/ssc/data/analysis/scitools/overview.html.

[56] Photons pair-converting in the top 12 layers of the tracker are classified as *front*-converting photons, while all others are classified as *back*-converting.

[57] The test statistics (or TS) is defined as $\mathrm{TS} = -2(\ln L_0 - \ln L_1)$, where L_0 and L_1 are the likelihoods of the background (null hypothesis) and the hypothesis being tested (e.g., source plus background). According to Wilks (1938), the significance of a detection is approximately $n_\sigma = \sqrt{(\mathrm{TS})}$ (see also Ajello et al. 2008).

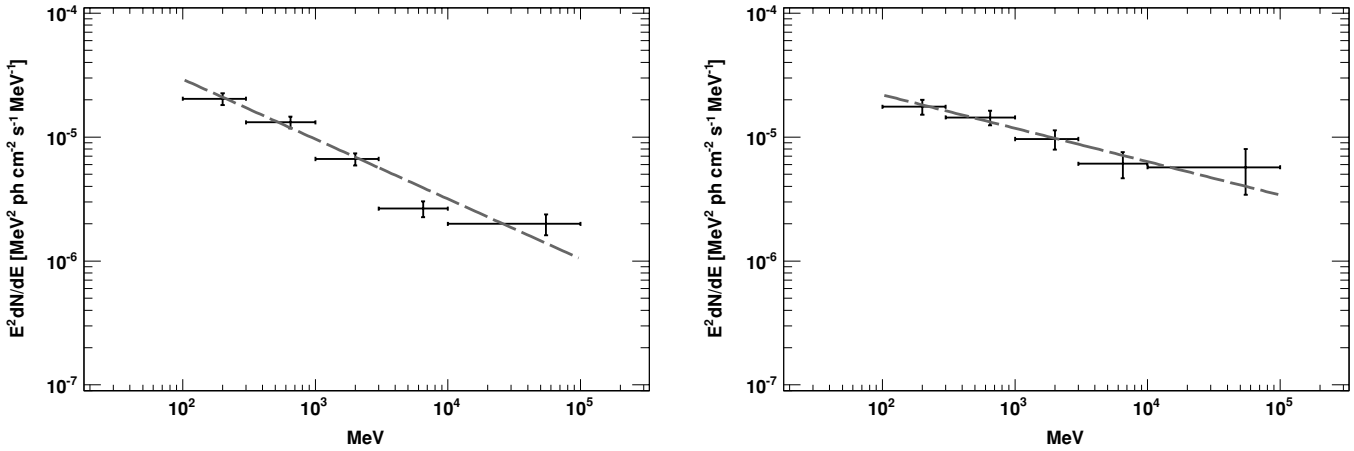

Figure 3. Stacked spectrum of FSRQs (left) and BL Lac objects (right) in the *Fermi*-LAT *flux-limited* sample.

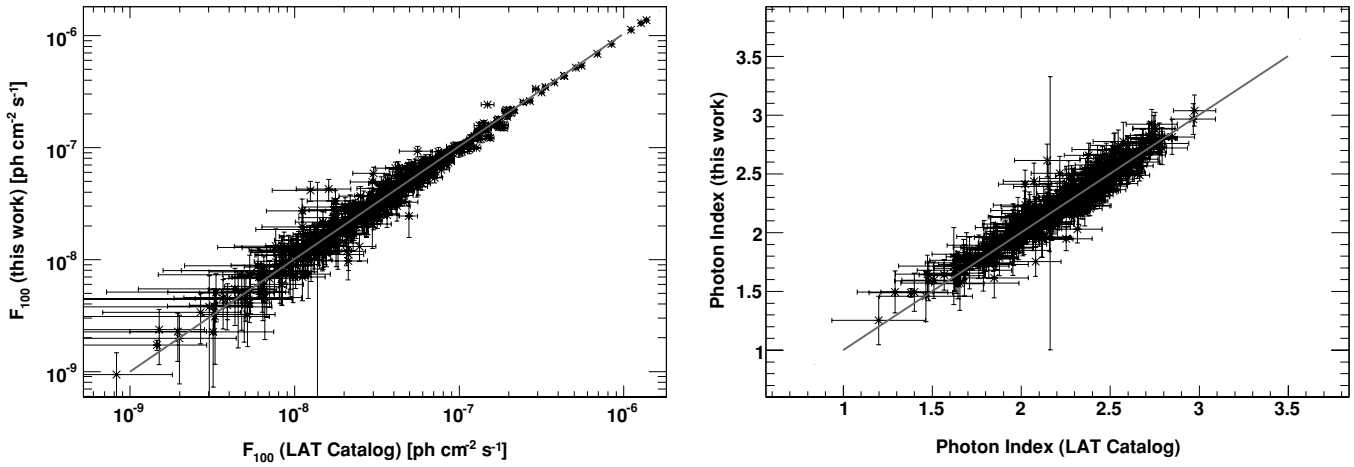

Figure 4. Performance of the detection pipeline used in this work with respect to the detection pipeline used in Abdo et al. (2010b). The left panel shows the comparison of the reconstructed γ-ray fluxes, while the right panel shows the comparison of the photon indices. In both cases, the solid line shows the locus of points for which the quantity reported in the y-axis equals the one in the x-axis.

100 MeV–100 GeV data, is not reported in Abdo et al. (2010b), but it can be readily obtained using the following expression:

$$F_{100} = E_{\rm piv} \times F_{\rm density} \times \left(\frac{100}{E_{\rm piv}}\right)^{1-\Gamma} \times |1-\Gamma|^{-1}, \qquad (1)$$

where F_{100} is the 100 MeV–100 GeV photon flux, Γ is the absolute value of the photon index, $E_{\rm piv}$ is the pivot energy, and $F_{\rm density}$ is the flux density at the pivot energy (see Abdo et al. 2010b, for details). Figure 4 shows the comparisons of both fluxes (above 100 MeV) and of the photon indices for the sources detected in both pipelines. It is clear that the fluxes and photon indices derived in this analysis are reliable; for each source, they are consistent with those in Abdo et al. (2010b) within the reported errors.

The number of sources detected in the simplified pipeline is smaller than that found by Abdo et al. (2010b). Above a TS of 50 and $|b| \geqslant 20^\circ$, our approach detects 425 sources while the 1FGL catalog has 497. Indeed, our aim is not to produce a detection algorithm that is as sensitive as the one used in Abdo et al. (2010b), but a detection algorithm that is proven to be reliable and can be consistently applied to both real data and simulations. This allows us to properly assess all selection effects important for the LAT survey and its analysis. On this note, we remark that all the 425 sources detected by our pipeline are also detected by Abdo et al. (2010b). For this reason, we limit the studies presented in this work to the subsample of sources which is detected by our pipeline. The details of this sample of sources are reported in Table 2. The associations are the ones reported in Abdo et al. (2010e) and Abdo et al. (2010b). In our sample, 161 sources are classified as FSRQs and 163 as BL Lac objects, while only 4 as blazars of uncertain classification. The number of sources which are unassociated is 56, thus the identification incompleteness of this sample is $\sim 13\%$.

4.2. Derivation of the Sky Coverage

In order to derive the sky coverage from simulations, detected sources (output) need to be associated to the simulated ones (input). We do this on a statistical basis using an estimator which is defined for each set of input–output sources as

$$R^2 = \left(\frac{||\bar{x} - \bar{x_0}||}{\sigma_{\rm pos}}\right)^2 + \left(\frac{S - S_0}{\sigma_S}\right)^2 + \left(\frac{\Gamma - \Gamma_0}{\sigma_\Gamma}\right)^2, \qquad (2)$$

where $\bar{x}$, S, and Γ are the source coordinates, fluxes, and photon indices as determined from the ML step while $\bar{x_0}$, S_0, and Γ_0 are the simulated (input) values. The 1σ errors on the position, flux, and photon index are $\sigma_{\rm pos}$, σ_S, and σ_Γ, respectively. We then flagged as the most likely associations those pairs with the minimum value of R^2. All pairs with an angular separation that

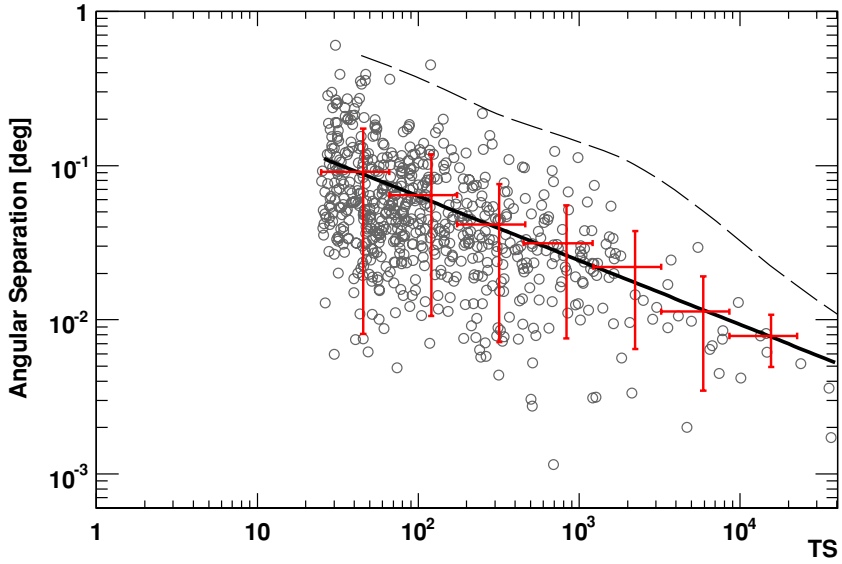

Figure 5. Angular separation of the real LAT sources from the most probable associated counterpart as a function of TS. All sources with $|b| \geqslant 10^{\circ}$, with a probability of associations larger than 0.5, were used (see Abdo et al. 2010e, for a definition of probability of association). The solid line is the best fit for the mean offset of the angular separations, while the dashed line represents the observed 5σ error radius as a function of test statistics. Note that the 5σ error radius is weakly dependent on the level of probability of association chosen.

(A color version of this figure is available in the online journal.)

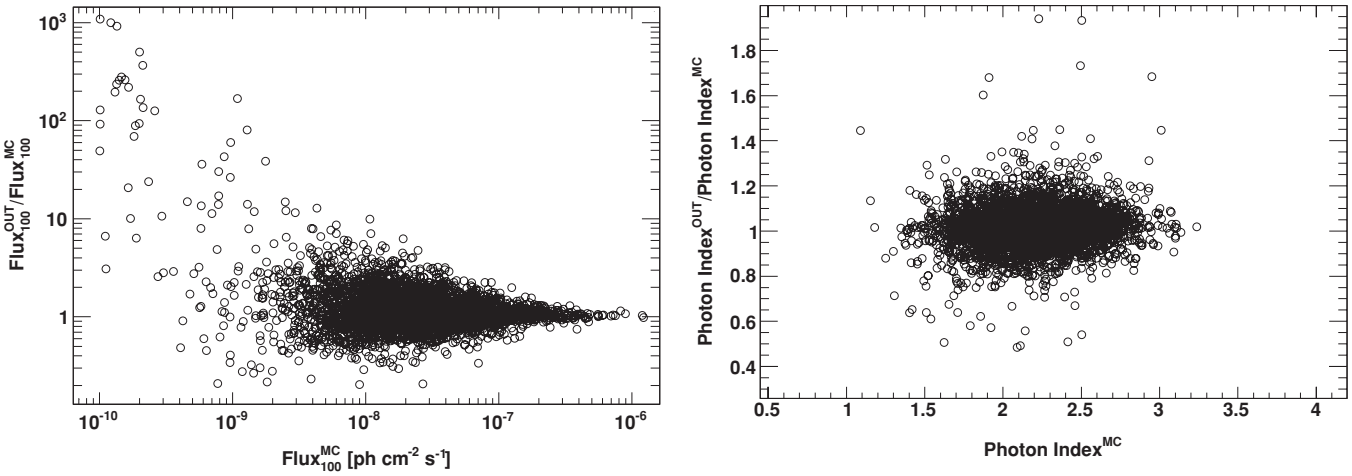

Figure 6. Left panel: reconstructed vs. simulated fluxes for all sources with TS $\geqslant$ 50 and $|b| \geqslant 20^{\circ}$. For the analysis reported here, only sources with $F_{100} \geqslant 10^{-9}$ ph cm^{-2} s^{-1} are considered. Right panel: reconstructed vs. simulated photon indices for all sources with TS $\geqslant$ 50 and $|b| \geqslant 20^{\circ}$.

Table 2
Composition of the $|b| \geqslant 20$ TS $\geqslant 50$ Sample Used in this Analysis

CLASS	No. of Objects
Total	425
FSRQs	161
BL Lac objects	163
Uncertain[a]	4
Blazar candidates	24
Radio galaxies	2
Pulsars	9
Others[b]	6
Unassociated sources	56

Notes.
[a] Blazars with uncertain classification.
[b] It includes starburst galaxies, narrow-line Seyfert 1 objects, and Seyfert galaxy candidates.

is larger than the 4σ error radius are flagged as spurious and excised from the following analysis. The empirical, as derived from the real data, 5σ error radius as a function of source TS is shown in Figure 5. As in Hasinger et al. (1993) and in Cappelluti et al. (2007), we defined *confused* sources for which the ratio $S/(S_0 + 3\sigma_S)$ (where σ_S is the error on the output flux) is larger than 1.5. We found that, according to this criterion, ~4% of the sources (detected for $|b| \geqslant 10^{\circ}$) are confused in the first year survey.

The right panel of Figure 6 shows the ratio of reconstructed to simulated source flux versus the simulated source flux. At medium to bright fluxes, the distribution of the ratio is centered on unity showing that there are no systematic errors in the flux measurement. At low fluxes (in particular, for $F_{100} < 10^{-9}$ ph cm^{-2} s^{-1}), the distribution is slightly (or somewhat) biased toward values greater than unity. This is produced by three effects: (1) source confusion, (2) Eddington bias (Eddington 1940), and (3) non-converging ML fits (see Section 5.1 for details). The Eddington bias arises from measurement errors of any intrinsic source property (e.g., source flux). Given its nature, it affects only sources close to the

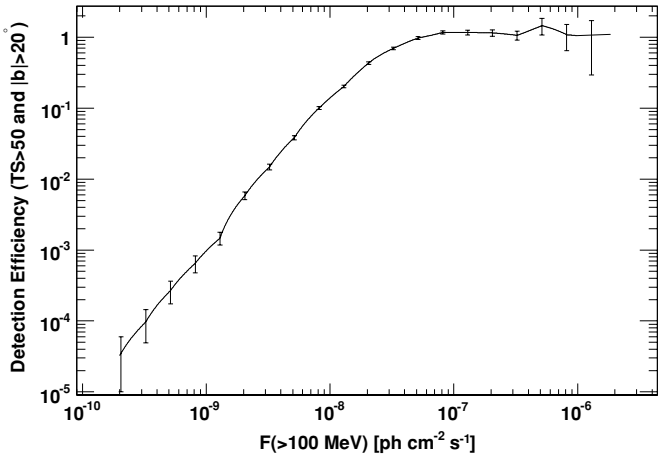

Figure 7. Detection efficiency as a function of measured source flux for $|b| \geqslant 20^\circ$, TS $\geqslant$ 50, and a sample of sources with a mean photon index of 2.40 and dispersion of 0.28. The error bars represent statistical uncertainties from the counting statistic of our Monte Carlo simulations.

detection threshold. Indeed, at the detection threshold, the uncertainty in the reconstructed fluxes makes sources with a measured flux slightly larger than the real value more easily detectable in the survey, rather than those with a measured flux slightly lower than the real one. This causes the shift of the flux ratio distribution of Figure 6 to move systematically to values larger than unity at low fluxes. In any case, the effect of this bias is not relevant as it affects less than 1% of the entire population. This uncertainty will be neglected as only sources with $F_{100} \geqslant 10^{-9}$ ph cm^{-2} s^{-1} will be considered for the analysis presented here. Moreover, the right panel of Figure 6 shows that the measured photon index agrees well with the simulated one.

In addition to assessing the reliability and biases of our source detection procedure, the main aim of these simulations is to provide a precise estimate of the completeness function of the *Fermi*/LAT survey (known also as sky coverage). The one-dimensional sky coverage can be derived for each bin of flux as the ratio between the number of detected sources and the number of simulated sources. The detection efficiency for the entire TS $\geqslant$ 50 and $|b| \geqslant 20^\circ$ sample is reported in Figure 7. This plot shows that the LAT sensitivity extends all the way to $F_{100} \sim 10^{-10}$ ph cm^{-2} s^{-1} although at those fluxes only the hardest sources can be detected. Also the sample becomes complete for $F_{100} = (7\text{–}8) \times 10^{-8}$ ph cm^{-2} s^{-1}. Since for these simulations the *intrinsic* distribution of photon indices has been used (see, e.g., Section 3.1), this sky coverage properly takes into account the bias toward the detection of hard sources. This also means that this sky coverage cannot be applied to other source samples with very different photon-index distributions.

5. SYSTEMATIC UNCERTAINTIES

5.1. Non-converging ML Fits

A small number of sources detected by our pipeline have unreliable spectral fits. Most of the time, these sources have a reconstructed photon index that is very soft (e.g., ∼5.0) and at the limit of the accepted range of values. As a consequence, their reconstructed flux overestimates the true flux by up to factor 1000 (see the left panel of Figure 6). This is due to the fact the ML algorithm does not find an absolute minimum of the fitting function for these cases. Inspection of the regions of interests (ROIs) of these objects shows that this tends to happen either in regions very dense with sources or close to the Galactic plane, where the diffuse emission is the brightest. The best approach in this case would be to adopt an iterative procedure for deriving the best-fitting parameters which starts by optimizing the most intense components (e.g., diffuse emissions and bright sources) and then move to the fainter ones. This procedure is correctly implemented in Abdo et al. (2010b). Its application to our problem would make the processing time of our simulations very long, and we note that the systematic uncertainty deriving from it is small. Indeed, the number of sources with unreliable spectral parameters for TS $\geqslant$ 25 are 2.3% and 2.0% for $|b| \geqslant 15^\circ$ and $|b| \geqslant 20^\circ$, respectively. These fractions decrease to 1.2% and 0.9% adopting TS $\geqslant$ 50.

To limit the systematic uncertainties in this analysis, we will thus select only those sources which are detected above TS $\geqslant$ 50 and $|b| \geqslant 20^\circ$. It will also be shown that results do not change if the sample is enlarged to include all sources with $|b| \geqslant 15^\circ$.

5.2. Variability

It is well known that blazars are inherently variable objects with variability in flux of up to a factor 10 or more. Throughout this work, only average quantities (i.e., mean flux and mean photon index) are used. This is correct in the context of the determination of the mean energy release in the universe of each source. Adopting the peak flux (i.e., the brightest flux displayed by each single source) would produce the net effect of overestimating the true intrinsic source density at any flux (see the examples in Reimer & Thompson 2001) with the result of overestimating the contribution of sources to the diffuse background.

It is not straightforward to determine how blazar variability affects the analysis presented here. On timescales large enough (such as the one spanned by this analysis), the mean flux is a good estimator of the mean energy release of a source. This is not true on short timescales (e.g., ∼1 month), since the mean flux corresponds to the source flux at the moment of the observation. The continuous scanning of the γ-ray sky performed by *Fermi* allows the determination of long-term variability with unprecedented accuracy. As already shown in Abdo et al. (2009a), the picture arising from *Fermi* is rather different from the one derived by EGRET (Hartman et al. 1999). Indeed, the peak-to-mean flux ratio for *Fermi* sources is considerably smaller than that for EGRET sources. For most of the *Fermi* sources, this is just a factor 2, as is confirmed in the one year sample (see Figure 10 in Abdo et al. 2010e). This excludes the possibility that most of the sources are detected because of a single outburst which happened during the 11 months of observation and are undetected for the remaining time. Moreover, as shown in Abdo et al. (2010c), there is little or no variation of the photon index with flux. We thus believe that no large systematic uncertainties are derived from the use of average physical quantities, and the total systematic uncertainty (see the next section) will be slightly overestimated to accommodate possible uncertainties caused by variability.

5.3. Non-power-law Spectra

It is well known that the spectra of blazars are complex and often show curvature when analyzed over a large wave band. In this case, the approximation of their spectrum with a simple power law (in the 0.1–100 GeV band) might provide a poor estimate of their true flux. To estimate the uncertainties derived by this assumption, we plotted for the extragalactic sample used here (e.g., TS $\geqslant$ 50 and $|b| \geqslant 20^\circ$) the source

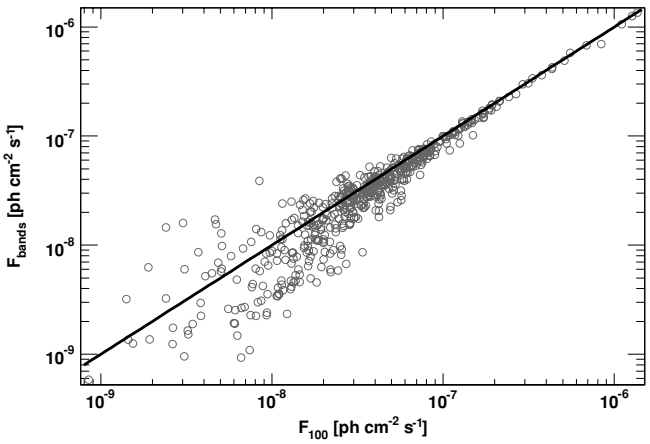

Figure 8. Source flux estimated with a power-law fit to the 0.1–100 GeV band vs. the sum of the source fluxes derived in five contiguous energy bands (see Abdo et al. 2010b, for details). The solid line is the $F_{\rm bands} = F_{100}$ relation. The spread at low fluxes arises from the difficulties of estimating the source flux in small energy bands.

flux as derived from the power-law fit to the whole band versus the source flux as derived from the sum of the fluxes over the five energy bands reported in Abdo et al. (2010b). This comparison is reported in Figure 8. From the figure, it is apparent that the flux (F_{100}) derived from a power-law fit to the whole band slightly overestimates the true source flux. Analysis of the ratio between the power-law flux and the flux derived in five energy bands shows that, on average, the F_{100} flux overestimates the true source flux by ∼8%. At very bright fluxes (e.g., $F_{100} \geqslant 10^{-7}$ ph cm^{-2} s^{-1}), the overestimate reduces to ∼5%. For the analysis presented here, we will thus assume that the total systematic uncertainty connected to the use of fluxes computed with a power-law fit over the broad 0.1–100 GeV band is 8%.

Considering also the uncertainties of the previous sections, we derive that the total systematic uncertainty for the sample used here (TS $\geqslant$ 50 and $|b| \geqslant 20^\circ$) is ∼10%. Since this uncertainty mostly affects the determination of the source flux, it will be propagated by shifting in flux the sky coverage of Figure 7 by ±10%.

6. SOURCE COUNT DISTRIBUTIONS

The source count distribution, commonly referred to as log N–log S or size distribution, is the cumulative number of sources $N(> S)$ detected above a given flux S. In this section, we apply several methods to derive the source count distribution of *Fermi*/LAT sources. We also remark that the catalog used for this analysis is the one described in Section 4.1 (see also Table 2).

6.1. Standard Approach

A standard way to derive the (differential) log N–log S is through the following expression:

$$\frac{dN}{dS} = \frac{1}{\Delta S} \sum_{i=1}^{N_{\Delta S}} \frac{1}{\Omega_i}, \tag{3}$$

where $N_{\Delta S}$ is the total number of detected sources with fluxes in the ΔS interval, and Ω_i is the solid angle associated with the flux of the $i_{\rm th}$ source (i.e., the detection efficiency multiplied by the survey solid angle). We also note that formally N is an areal density and should be expressed as $dN/d\Omega$. However, for simplicity of notation the areal density will, throughout this paper, be expressed as N. For the $|b| \geqslant 20^\circ$ sample, the geometric solid angle of the survey is 27143.6 deg^2. In each flux bin, the final uncertainty is obtained by summing in quadrature the error on the number of sources and the systematic uncertainties described in Section 5.

Both the differential and the cumulative version of the source count distributions are reported in Figure 9. In order to parameterize the source count distribution, we perform a χ^2 fit to the differential data using a broken power-law model of the type:

$$\begin{aligned} \frac{dN}{dS} &= AS^{-\beta_1}, && S \geqslant S_b; \\ &= AS_b^{-\beta_1+\beta_2} S^{-\beta_2}, && S < S_b; \end{aligned} \tag{4}$$

where A is the normalization and S_b is the flux break. The best-fit parameters are reported in Table 3. The log N–log S distribution of GeV sources shows a strong break ($\Delta\beta = \beta_1 - \beta_2 \approx 1.0$) at $F_{100} = 6.97(\pm 0.13) \times 10^{-8}$ ph cm^{-2} s^{-1}. At fluxes brighter than the break flux, the source count distribution is consistent with Euclidean ($\beta_1 = 2.5$), while it is not at fainter fluxes. As Table 3 shows, these results do not change if the sample under study is enlarged to $|b| \geqslant 15^\circ$.

6.2. A Global Fit

Because of the spectral selection effect discussed in Section 3.1, the sky coverage derived in Section 4.2 can be

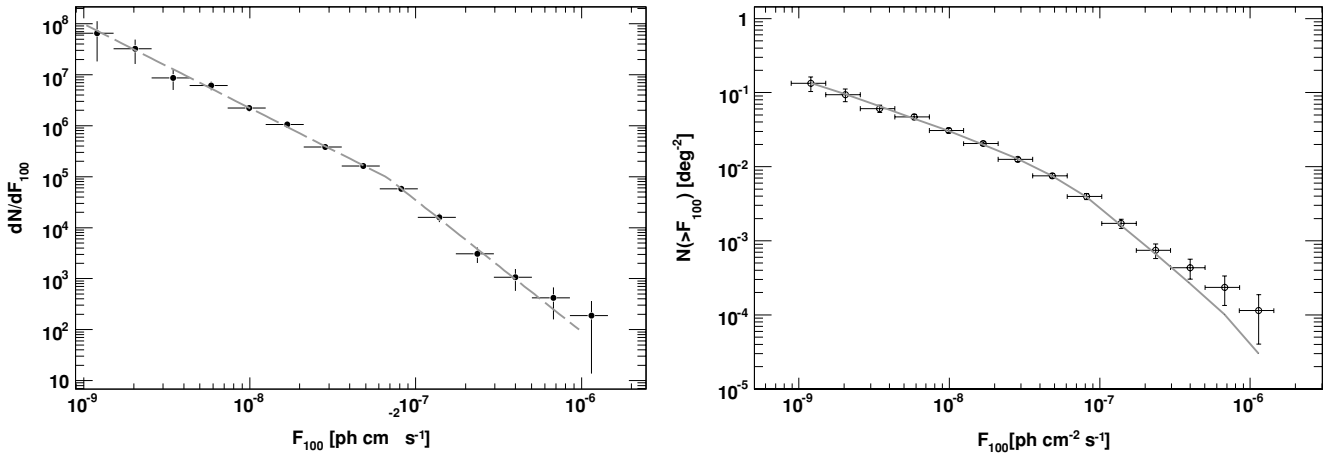

Figure 9. Differential (left) and cumulative (right) log N–log S for all sources with TS $\geqslant$ 50 and $|b| \geqslant 20^\circ$. The dashed line is the best-fit broken power-law model as reported in the text.

Table 3
Results of the Power-law Fits to the Differential Source Count Distributions Obtained with the Standard Method of Section 6.1

SAMPLE	No. of Objects	Sample Limits		Best-fit Parameters			
		TS $\geqslant$	$\lvert b\rvert \geqslant$	A^{a}	β_1	$S_b{}^{b}$	β_2
ALL	425	50	20°	$1.15^{+0.15}_{-0.15}$	$2.63^{+0.22}_{-0.19}$	$6.97^{+1.28}_{-1.29}$	$1.64^{+0.06}_{-0.07}$
ALL	483	50	15°	$1.74^{+0.16}_{-0.16}$	$2.60^{+0.19}_{-0.17}$	$6.40^{+1.04}_{-1.08}$	$1.60^{+0.06}_{-0.07}$

Notes.
[a] In units of 10^{-14} cm^2 s deg^{-2}.
[b] In units of 10^{-8} ph cm^{-2} s^{-1} ($0.1 \leqslant E \leqslant 100$ GeV).

used only with samples that have a distribution of the photon indices similar to the one used in the simulations (i.e., a Gaussian with mean and dispersion of 2.40 and 0.28). Here, we aim at overcoming this limitation by implementing for the first time a novel, more formal, analysis to derive the source count distribution. We aim at describing the properties of the sample in terms of a distribution function of the following kind:

$$\frac{dN}{dSd\Gamma} = f(S) \cdot g(\Gamma), \tag{5}$$

where $f(S)$ is the intrinsic flux distribution of sources and $g(\Gamma)$ is the intrinsic distribution of the photon indices. In this analysis, $f(S)$ is modeled as a double power-law function as in Equation (4). The index distribution $g(\Gamma)$ is modeled as a Gaussian function:

$$g(\Gamma) = e^{-\frac{(\Gamma-\mu)^2}{2\sigma^2}}, \tag{6}$$

where μ and σ are, respectively, the mean and the dispersion of the Gaussian distribution. As it is clear from Equation (5), we made the hypothesis that the $dN/dSd\Gamma$ function is factorizable in two separate distributions in flux and photon index. This is the simplest assumption that could be made and as it will be shown in the next sections it provides a good description of the data. Moreover, we emphasize, as already did in Section 4, that this analysis implicitly assumes that the photon-index distribution does not change with flux. This will be discussed in more detail in the next sections.

This function is then fitted to all data points using an ML approach as described in Section 3.2 of Ajello et al. (2009). In this method, the likelihood function can be defined as

$$L = \exp(-N_{\rm exp}) \prod_{i=1}^{N_{\rm obs}} \lambda(S_i, \Gamma_i), \tag{7}$$

with $\lambda(S, \Gamma)$ defined as

$$\lambda(S, \Gamma) = \frac{dN}{dSd\Gamma} \Omega(S, \Gamma), \tag{8}$$

where $\Omega(S, \Gamma)$ is the photon-index-dependent sky coverage and $N_{\rm obs}$ is the number of observed sources. This is generated from the same Monte Carlo simulation of Section 4 with the difference that this time the detection probability is computed for each bin of the photon-index–flux plane as the ratio between detected and simulated sources (in that bin). This produces a sky coverage which is a function of both the source flux and the photon index.

The *expected* number of sources $N_{\rm exp}$ can be computed as

$$N_{\rm exp} = \int d\Gamma \int dS \lambda(S, \Gamma). \tag{9}$$

The ML parameters are obtained by minimizing the function $C(= -2\ln L)$:

$$C = -2 \sum_{i}^{N_{\rm obs}} \ln(\lambda(S_i, \Gamma_i)) - 2N \ln(N_{\rm exp}), \tag{10}$$

while their associated 1σ errors are computed by varying the parameter of interest, while the others are allowed to float, until an increment of $\Delta C = 1$ is achieved. This gives an estimate of the 68% confidence region for the parameter of interest (Avni 1976).

Once the $dN/dSd\Gamma$ has been determined, the standard differential source count distribution can be readily derived as

$$\frac{dN}{dS} = \int_{-\infty}^{\infty} d\Gamma \frac{dN}{dSd\Gamma}. \tag{11}$$

6.3. The Total Sample of Point Sources

The results of the best-fit model for the entire sample of sources (for TS $\geqslant$ 50 and $|b| \geqslant 20°$) are reported in Table 4. Figure 10 shows how well the best-fit model reproduces the observed index and flux distributions. The χ^2-test yields that the probabilities that the real distribution and the model line come from the same parent population are 0.98 and 0.97 for the photon index and flux distributions, respectively. In Figure 11, the source count distribution obtained here is compared to the one derived using the standard approach of Section 6.1; the good agreement is apparent.

We also derived the source count distributions of all objects that are classified as blazars (or candidate blazars) in our sample. This includes 352 out of the 425 objects reported in Table 2. The number of sources that lack association is 56 and thus the incompleteness of the blazar sample is $56/425 \approx 13\%$. A reasonable and simple assumption is that the 56 unassociated sources are distributed among the different source classes in a similar way as the associated portion of the sample (see Table 2). This means that 46 out of the 56 unassociated sources are likely to be blazars. As it is possible to notice both from the best-fit parameters of Table 4 and from Figure 12, there is very little difference between the source count distributions of the entire sample and the one of blazars. This confirms on a statistical basis that most of the 56 sources without association are likely to be blazars. It is also clear from Figure 10 that the model (e.g., Equation (5)) represents a satisfactory description of the data. This also implies that the *intrinsic* photon-index distribution of blazars is compatible with a Gaussian distribution that does not change (at least dramatically) with source flux in the range of fluxes spanned by this analysis. A change in the average spectral properties of blazars with flux (and/or redshift) might be caused by the different cosmological evolutions of FSRQs and BL Lac objects or by the spectral evolution of the two source classes with

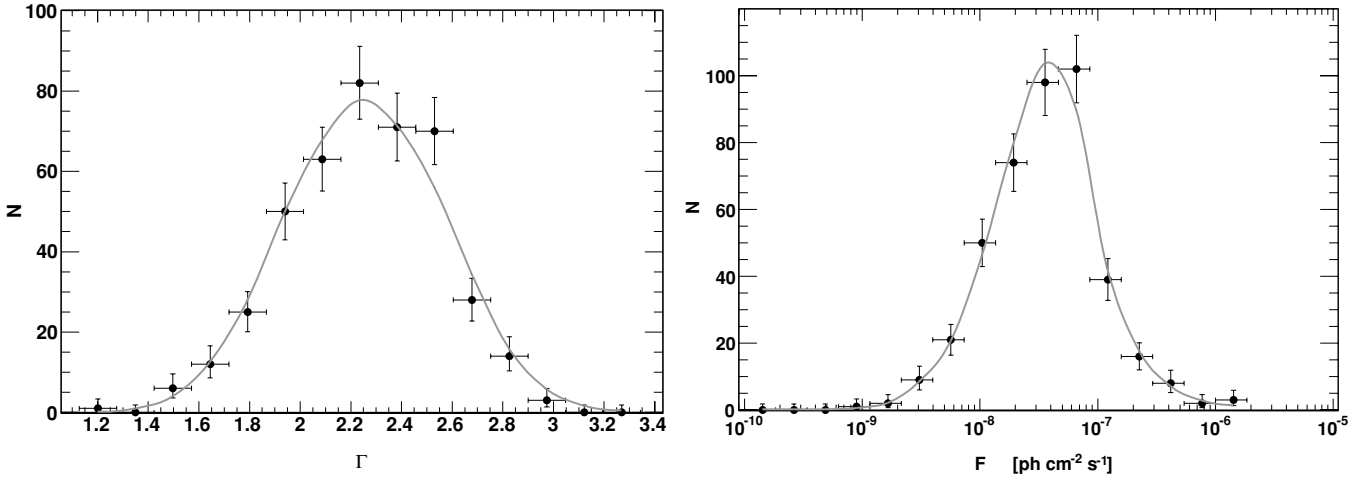

Figure 10. Distribution of photon indices (left) and fluxes (right) for the TS $\geqslant 50$ and $|b| \geqslant 20^\circ$ sources. The dashed line is the best-fit $dN/dSd\Gamma$ model. Using the χ^2 test, the probabilities that the data and the model line come from the same parent population are 0.98 and 0.97 for the photon-index and flux distributions, respectively.

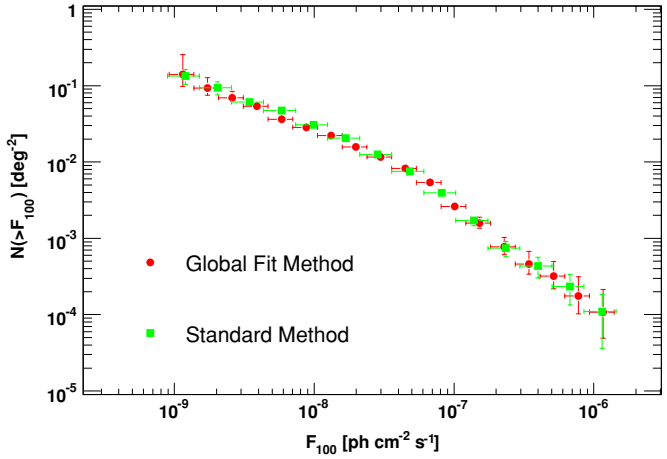

Figure 11. Comparison of $\log N$–$\log S$ of the whole sample of (TS $\geqslant 50$ and $|b| \geqslant 20^\circ$) sources built with the standard method (green data points; see Section 6.1) and the global fit method (red data points; see Section 6.2).

(A color version of this figure is available in the online journal.)

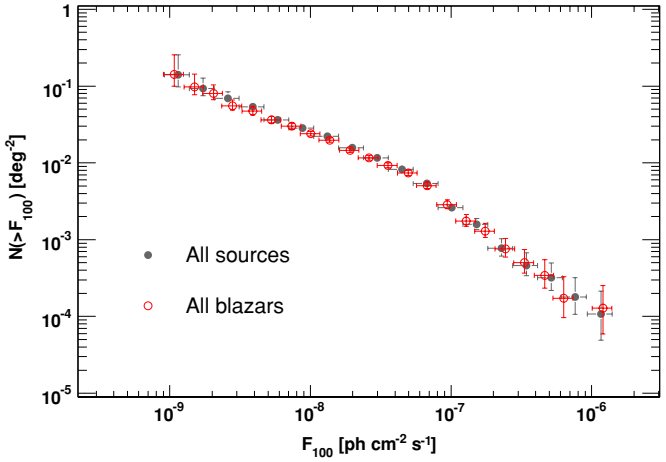

Figure 12. Comparison between $\log N$–$\log S$ distributions of the whole sample of sources (solid circles) and blazars (open circles). The solid lines are the respective best-fit models as reported in Table 4.

(A color version of this figure is available in the online journal.)

redshift. While it is something reasonable to expect, this effect in the current data set is not observed. The luminosity function, which is left to a future paper, will allow us to investigate this effect in great detail.

6.4. FSRQs

For the classification of blazars as FSRQs or BL Lac objects, we use the same criteria adopted in Abdo et al. (2009a). This classification relies on the conventional definition of BL Lac objects outlined in Stocke et al. (1991), Urry & Padovani (1995), and Marcha et al. (1996) in which the equivalent width of the strongest optical emission line is <5 Å and the optical spectrum shows a Ca II H/K break ratio C < 0.4.

It is important to correctly determine the incompleteness of the sample when dealing with a subclass of objects. Indeed, in the sample of Table 2, 56 objects have no associations and 28 have either an uncertain or a tentative association with blazars. Thus, the total incompleteness is $84/425 = \sim 19\%$ when we refer to either FSRQs or BL Lac objects separately. The incompleteness levels of all the samples used here are also reported in Table 4 for clarity. Since we did not perform dedicated simulations for the FSRQ and the BL Lac object classes, their source count distributions can be derived only with the method described in Section 6.2.

The best fit to the source counts (reported in Table 4) is a double power-law model with a bright-end slope of 2.41 ± 0.16 and faint-end slope 0.70 ± 0.30. The $\log N$–$\log S$ relationship shows a break around $F_{100} = 6.12(\pm 1.30) \times 10^{-8}$ ph cm^{-2} s^{-1}. The intrinsic distribution of the photon indices of FSRQs is found to be compatible with a Gaussian distribution with a mean and a dispersion of 2.48 ± 0.02 and 0.18 ± 0.01, respectively, in agreement with what found previously in Table 1. The faint-end slope is noticeably flatter and this might be due to the fact that many of the unassociated sources below the break might be FSRQs. Figure 13 shows how the best-fit model reproduces the observed photon-index and flux distributions. The χ^2-test indicates that the probability that the real distribution and the model line come from the same parent population is $\geqslant 0.99$ for both the photon-index and flux distributions, respectively. The left panel shows that the photon-index distribution is not reproduced perfectly. This might be due to incompleteness or by the fact that the intrinsic distribution of photon indices is actually not Gaussian. However, a Kolmogorov–Smirnov (K-S) test between the predicted and the observed distribution yields

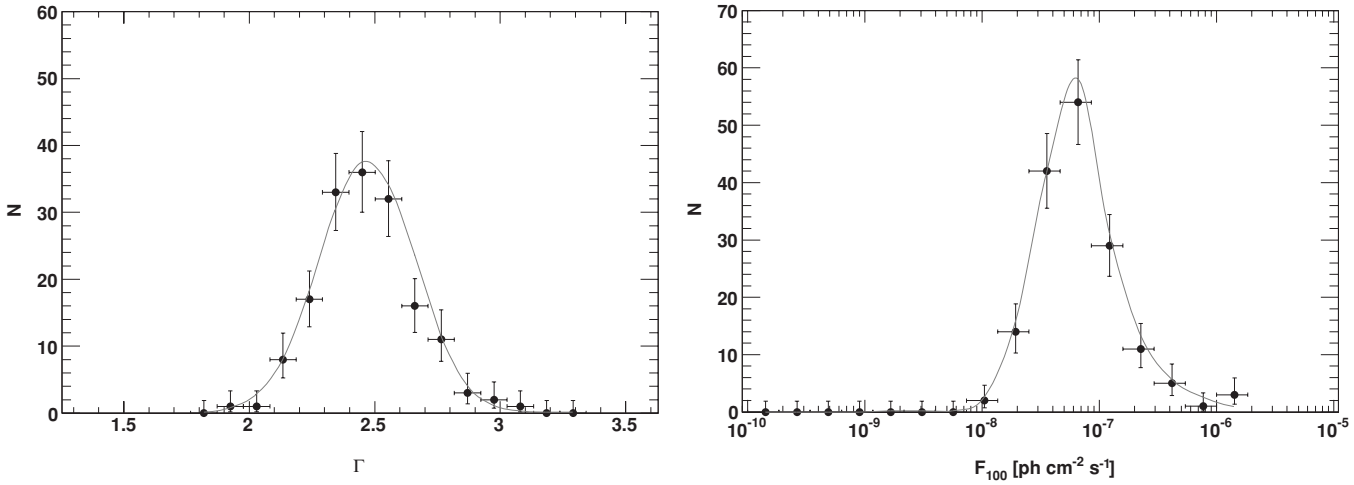

Figure 13. Distribution of photon indices (left) and fluxes (right) for the TS $\geqslant$ 50 and $|b| \geqslant 20^\circ$ sources associated with FSRQs.

Table 4
Results of the Best Fits to the Source Count Distributions

SAMPLE	No. of Objects	Incompl.	Sample Limits		Best-fit Parameters					
			TS $\geqslant$	$\lvert b\rvert \geqslant$	A[a]	β_1	S_b[b]	β_2	μ	σ
ALL	425	0	50	20°	16.46 ± 0.80	2.49 ± 0.12	6.60 ± 0.91	1.58 ± 0.08	2.36 ± 0.02	0.27 ± 0.01
BLAZAR	352	0.13	50	20°	18.28 ± 1.00	2.48 ± 0.13	7.39 ± 1.01	1.57 ± 0.09	2.37 ± 0.02	0.28 ± 0.01
FSRQ	161	0.19	50	20°	72.41 ± 5.76	2.41 ± 0.16	6.12 ± 1.30	0.70 ± 0.30	2.48 ± 0.02	0.18 ± 0.01
BL Lac object	163	0.19	50	20°	0.106 ± 0.009	2.74 ± 0.30	6.77 ± 1.30	1.72 ± 0.14	2.18 ± 0.02	0.23 ± 0.01
Unassociated	56	0	50	20°	3.12(±0.5) × 10^{-5}	3.16 ± 0.50	4.48 ± 1.3	1.63 ± 0.24	2.29 ± 0.03	0.20

Notes.
[a] In units of 10^{-14} cm^2 s deg^{-2}.
[b] In units of 10^{-8} ph cm^{-2} s^{-1}.

that both distributions have a probability of ∼96% of being drawn from the same parent population. Thus, the current data set is compatible with the hypothesis that the intrinsic index distribution is Gaussian. The log N–log S of FSRQs is shown in Figure 14.

6.5. BL Lac Objects

The best-fit model of the source count distribution of the 161 BL Lac objects is again a broken power-law model. The break is found to be at $F_{100} = (6.77 \pm 1.30) \times 10^{-8}$ ph cm^{-2} s^{-1} while the slopes below and above the break are 1.72 ± 0.14 and 2.74 ± 0.30, respectively. The intrinsic photon-index distribution is found to be compatible with a Gaussian distribution with a mean and a dispersion of 2.18 ± 0.02 and 0.23 ± 0.01, respectively. These results are in good agreement with the ones reported in Table 1. The best-fit parameters to the source count distribution are reported in Table 4. Figure 15 shows how the best-fit model reproduces the observed photon-index and flux distributions. The χ^2-test indicates that the probability that the real distribution and the model line come from the same parent population is $\geqslant$0.99 for both the photon-index and flux distributions, respectively. The log N–log S of BL Lac objects, compared to the one of FSRQs and blazars, is shown in Figure 14.

6.6. Unassociated Sources

We also constructed the log N–log S of the 56 sources that are unassociated, and it is reported in Figure 14. Their source count distribution displays a very steep bright-end slope ($\beta_1 = 3.16 \pm 0.50$), a break around ∼4.5 ×10^{-8} ph cm^{-2} s^{-1}, and a faint-end slope of 1.63 ± 0.24. The intrinsic photon-index distribution is found to be compatible with a Gaussian distribution with a mean and a dispersion of 2.29 ± 0.03 and 0.20 ± 0.01, respectively (see Table 4 for details). The extremely steep bright-end slope is caused by the fact that most (but not all) of the brightest sources have an association. Below the break, the log N–log S behaves like that of the blazars with the difference that the index distribution is suggesting that probably most of the sources are BL Lac objects. Indeed, as can be seen in Figure 14, all the sources with $F_{100} \leqslant 4 \times 10^{-8}$ ph cm^{-2} s^{-1} are identified as BL Lac objects in our sample.

6.7. Unfolding Analysis

Finally, we employ a different approach to evaluate the log N–log S distribution based on a deconvolution (unfolding) technique. This method allows reconstructing the distribution of the number of sources from the data without assuming any model, also taking into account the finite resolution (i.e., dispersion) of the sky coverage.

The purpose of the unfolding is to estimate the true distribution (cause) given the observed one (effect), and assuming some knowledge about the eventual migration effects (smearing matrix), as well as the efficiencies. The elements of the smearing matrix represent the probabilities to observe a given effect that falls in an observed bin Effect$_j$ from a cause in a given true bin Cause$_i$. In our case, the observed distribution represents the number of sources as a function of the observed flux above

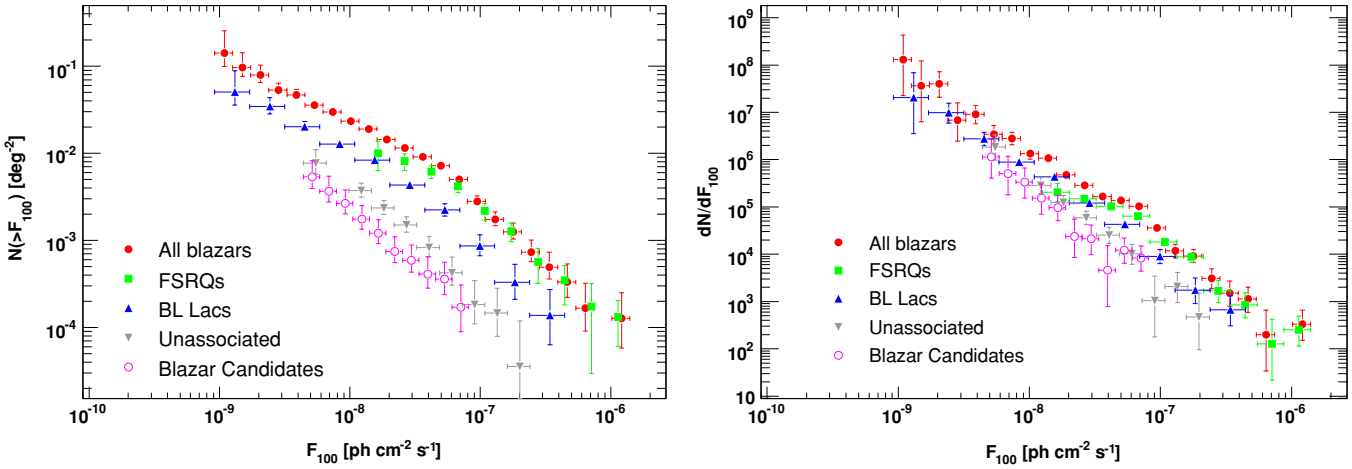

Figure 14. Cumulative (left) and differential (right) source count distributions of *Fermi* blazars and the subsamples reported in Table 4. Given the selection effect toward spectrally hard sources, BL Lac objects are detected to fluxes fainter than FSRQs. The flattening at low fluxes of the FSRQs $\log N$–$\log S$ is probably due to incompleteness (see the text for details). The "All Blazars" class also includes all of those sources which are classified as blazar candidates (see Table 2 for details).
(A color version of this figure is available in the online journal.)

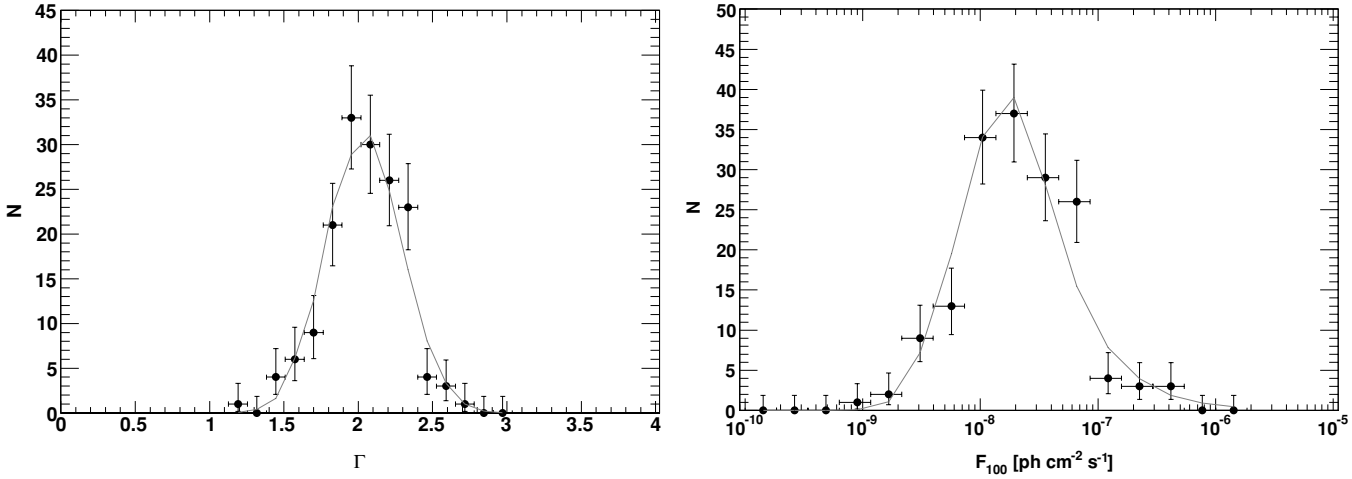

Figure 15. Distribution of photon indices (left) and fluxes (right) for the TS $\geqslant 50$ and $|b| \geqslant 20^\circ$ sources associated with BL Lac objects. The dashed line is the best-fit $dN/dSd\Gamma$ model.

100 MeV, while the true distribution represents the number of true sources as a function of the true flux above 100 MeV. The unfolding algorithm adopted here is based on the Bayes theorem (D'Agostini 1995).

The smearing matrix is evaluated using the Monte Carlo simulation described in the Section 4. Its elements, $P(\mathrm{F100}_{j,\mathrm{obs}}|\mathrm{F100}_{i,\mathrm{true}})$, represent the probabilities that a source with a true flux above 100 MeV, $\mathrm{F100}_{i,\mathrm{true}}$, is reconstructed with an observed flux above 100 MeV, $\mathrm{F100}_{j,\mathrm{obs}}$. The data are assumed to be binned in histograms. The bin widths and the number of bins can be chosen independently for the distribution of the observed and reconstructed variables.

The $\log N$–$\log S$ reconstructed with this method is shown in Figure 16, and it is apparent that the source count distributions derived with the three different methods are all in good agreement with each other.

6.8. Comparison with Previous Estimates

Figure 16 shows that the $\log N$–$\log S$ distributions displays a strong break at fluxes $F_{100} \approx 6 \times 10^{-8}$ ph cm^{-2} s^{-1}. This represents the first time that such a flattening is seen in the $\log N$–$\log S$ of γ-ray sources, blazar in particular. This is due to the fact that *Fermi* couples a good sensitivity to the all-sky coverage thus allowing to determine the source count distribution over more than three decades in flux.

Above fluxes of $F_{100} = 10^{-9}$ ph cm^{-2} s^{-1}, the surface density of sources is $0.12^{+0.03}_{-0.02}$ deg^{-2}. At these faint fluxes, our comparison can only be done with predictions from different models. Dermer (2007) and Inoue & Totani (2009) predict a blazar surface density of, respectively, 0.030 deg^{-2} and 0.033 deg^{-2}. Both of these predictions are a factor $\sim$4 below the LAT measurement. However, it should be stressed that these models are based on the EGRET blazar sample which, because of strong selection effects against high-energy photons, counted a very limited number of BL Lac objects.

At brighter fluxes ($F_{100} \geqslant 5 \times 10^{-8}$ ph cm^{-2} s^{-1}), Dermer (2007) predicts a density of FSRQs and BL Lac objects of 4.1×10^{-3} deg^{-2} and 1.1×10^{-3} deg^{-2}, respectively. At the same flux, Mücke & Pohl (2000) predict a density of 1.21×10^{-3} deg^{-2} and 3.04×10^{-4} deg^{-2} for FSRQs and BL Lac objects, respectively. The densities measured by *Fermi* are significantly larger, being $6.0(\pm 0.6) \times 10^{-3}$ deg^{-2} for FSRQs and $2.0(\pm 0.3) \times 10^{-3}$ deg^{-2} for BL Lac objects.

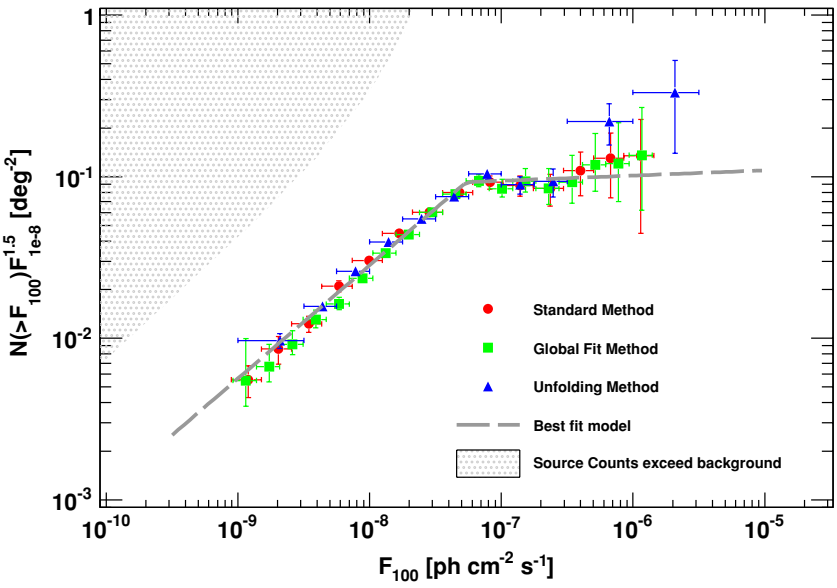

Figure 16. Source count distribution of *Fermi* pointlike sources derived with three different methods. The distribution has been multiplied by $(F_{100}/10^{-8})^{1.5}$. The dashed line is the best-fit model described in the text. The gray region indicates the flux at which a power law connecting the log N–log S break (at $\sim 6.6 \times 10^{-8}$ ph cm^{-2} s^{-1}) and that given flux exceeds the EGB emission (see the text for details).

(A color version of this figure is available in the online journal.)

7. ANALYSIS IN THE DIFFERENT ENERGY BANDS

The aim of the following analysis is to determine the contribution of point sources to the EGB in different contiguous energy bands. This is done by creating a log N–log S distribution in three different energy bands: 0.1–1.0 GeV, 1.0–10.0 GeV, and 10.0–100 GeV bands. This will allow us to study the spectrum of the unresolved emission from point sources and at the same time explore the properties of the source population in different bands. With this approach, the systematic uncertainty related to the flux estimate, given by the complex spectra of blazars (see Section 5.3), will be removed. In addition, use of these bands should allow us to extend the survey region to $|b| \geqslant 10^{\circ}$ (see Section 5.1).

The analysis follows the method outlined in Section 4 with the difference that the final ML fit is restricted to the band under investigation. In the spectral fit, all parameters (including the photon index) are left free and are optimized by maximizing the likelihood function. Only sources in a given band that have TS $\geqslant$ 25 are considered detected in that band. Formally, each band and related sample are treated as independent here and no prior knowledge of the source spectral behavior is assumed. In the three bands, the samples comprise, respectively, 362, 597, and 200 sources detected for $|b| \geqslant 10^{\circ}$ and TS $\geqslant$ 25.

In both the soft and the medium band (i.e., 0.1–1.0 GeV and 1.0–10.0 GeV, respectively), the log N–log S is well described by a double power-law model, while in the hardest band (10–100 GeV) the log N–log S is compatible with a single power-law model with a differential slope of 2.36 $\pm$ 0.07. The results of the best-fit models are reported in Table 5 and are shown in Figure 17. The *spectral bias* (see Section 2) is the strongest in the soft band while it is absent in the high-energy band, being already almost negligible above 1 GeV.

From the log N–log S in the whole band, we would expect (assuming a power law with a photon index of 2.4 and that the blazar population is not changing dramatically with energy) to find breaks at: 6.7×10^{-8}, 2.6×10^{-9}, and 1×10^{-10} ph cm^{-2} s^{-1} for the soft, medium, and hard bands, respectively. Indeed, these expectations are confirmed by the ML fits in the individual bands (e.g., see Table 5). The hard band constitutes the only exception, where the flux distribution barely extends below the flux at which the break might be observed.

The average spectral properties of the sample change with energy. We find that the *intrinsic* index distribution is compatible with a Gaussian distribution with means of 2.25 $\pm$ 0.02, 2.43 $\pm$ 0.03, and 2.17 $\pm$ 0.05. In the three bands, the fractions of BL Lac object-to-FSRQ are: 0.61, 1.14, and 3.53, respectively, with identification incompletenesses of 0.18, 0.25, and 0.25, respectively. It is apparent that the hardest band is the best one for studying BL Lac objects since the contamination due to FSRQs is rather small.

8. CONTRIBUTION OF SOURCES TO THE DIFFUSE BACKGROUND

The source count distribution can be used to estimate the contribution of pointlike sources to the EGB emission. This allows us to determine the fraction of the GeV diffuse emission that arises from pointlike source populations measured by *Fermi*. As specified in Section 2, this estimate does not include the contribution of sources that have been directly detected by *Fermi* since these are not considered in the measurement of the diffuse background. This estimate includes all of those sources that, because the detection efficiency changes with flux, photon index, and position in the sky, have not been detected.

The diffuse emission arising from a class of sources can be determined as

$$F_{\rm diffuse} = \int_{S_{\rm min}}^{S_{\rm max}} dS \int_{\Gamma_{\rm min}}^{\Gamma_{\rm max}} d\Gamma \frac{dN}{dS d\Gamma} S \left(1 - \frac{\Omega(\Gamma, S)}{\Omega_{\rm max}}\right), \quad (12)$$

where $\Omega_{\rm max}$ is the geometrical sky area and the $(1 - \Omega(\Gamma, S)/\Omega_{\rm max})$ term takes into account that the threshold at which LAT detects sources depends on both the photon index and the source flux. We note that neglecting the dependence of Ω on the photon index (i.e., using the mono-dimensional sky coverage reported in Figure 7) would result in an underestimate of

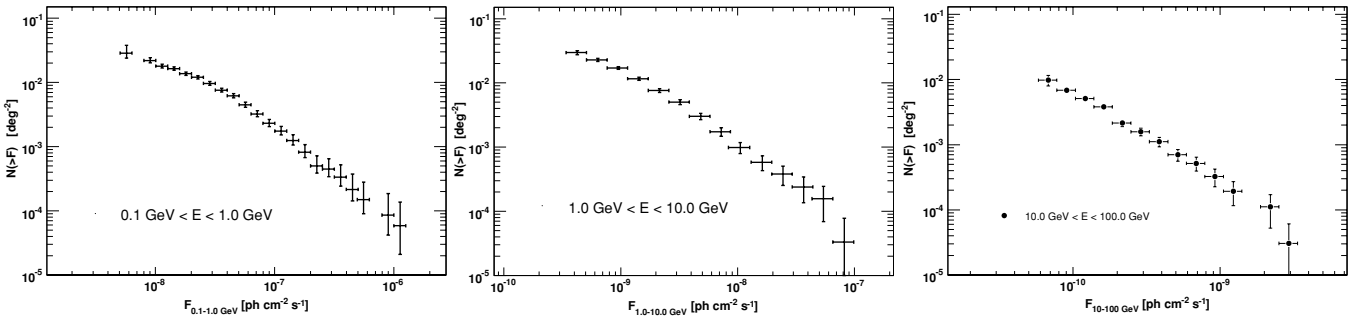

Figure 17. Source count distributions for the soft- (0.1–1.0 GeV; left), medium- (1.0–10.0 GeV; center), and high-energy (10.0–100.0 GeV; right) bands reconstructed with the method reported in Section 6.2.

Table 5
Results of the Best Fits to the Source Counts Distributions in Different Energy Bands

BAND	No. of Objects	Incompl.	Sample Limits		Best-fit Parameters					
			TS $\geqslant$	$\lvert b\rvert \geqslant$	A^a	β_1	$S_b{}^b$	β_2	μ	σ
0.1–1.0 GeV	362	0	25	10°	4.00 ± 0.21	$2.55^{+0.17}_{-0.22}$	$5.75^{+0.44}_{-2.22}$	$1.38^{+0.13}_{-0.46}$	$2.25^{+0.02}_{-0.02}$	$0.32^{+0.01}_{-0.01}$
1.0–10.0 GeV	597	0	25	10°	1.097 ± 0.05	$2.38^{+0.15}_{-0.14}$	0.23 ± 0.06	$1.52^{+0.8}_{-1.1}$	2.43	$0.40^{+0.02}_{-0.02}$
10.0–100.0 GeV	200	0	25	10°	$8.3(\pm 0.6)\times 10^{-3}$	$2.364^{+0.07}_{-0.07}$	...	...	2.17 ± 0.05	$0.82^{+0.05}_{-0.05}$
0.3–100.0 GeV	759	0	25	10°	5.33 ± 0.19	$2.44^{+0.15}_{-0.11}$	$1.69^{+0.33}_{-0.33}$	$1.70^{+0.06}_{-0.07}$	$2.35^{+0.02}_{-0.02}$	$0.30^{+0.01}_{-0.01}$

Notes. Parameters without an error estimate were kept fixed during the fitting stage.
[a] In units of 10^{-14} cm^2 s deg^{-2}.
[b] In units of 10^{-8} ph cm^{-2} s^{-1}.

the diffuse flux resolved by *Fermi* into point sources. The limits of integration of Equation (12) are $\Gamma_{\rm min} = 1.0$, $\Gamma_{\rm max} = 3.5$, and $S_{\rm max} = 10^{-3}$ ph cm^{-2} s^{-1}. We also note that the integrand of Equation (12) goes to zero for bright fluxes or for photon indices which are either very small or very large; thus, the integration is almost independent of the parameters reported above. The integration is not independent of the value of $S_{\rm min}$, which is set to the flux of the faintest source detected in the sample. For the analysis of the whole band $S_{\rm min} = 9.36 \times 10^{-10}$ ph cm^{-2} s^{-1}, while for the low, medium, and hard band $S_{\rm min}$ is set to 5.17 $\times 10^{-9}$ ph cm^{-2} s^{-1}, 3.58 $\times 10^{-10}$ ph cm^{-2} s^{-1}, and 6.11 $\times 10^{-11}$ ph cm^{-2} s^{-1}, respectively.

Since in the measurement of Abdo et al. (2010d), the sources that are subtracted are those detected in nine months of operation, the coverage used in Equation (12) is the one corresponding to the nine-month survey. The uncertainties on the diffuse flux have been computed by performing a bootstrap analysis. Integrating Equation (12), we find that the point source contribution is $1.63(\pm 0.18) \times 10^{-6}$ ph cm^{-2} s^{-1} sr^{-1}, where the systematic uncertainty is 0.6×10^{-6} ph cm^{-2} s^{-1} sr^{-1}. This corresponds to 16($\pm$1.8)% ($\pm$7% systematic uncertainty) of the isotropic diffuse emission measured by LAT (Abdo et al. 2010d) above 100 MeV. This small fraction is a natural consequence of the break of the source count distribution. However, it is also possible to show that the parameter space for the faint-end slope β_2 is rather limited and that a break must exist in the range of fluxes spanned by this analysis. Indeed, for a given β_2 (and all the other parameters of the log N–log S fixed at their best-fit values), one can solve Equation (12) to determine the flux at which the integrated emission of point sources exceeds the one of the EGB. Repeating this exercise for many different values of the β_2 parameter yields an exclusion region which constrains the behavior of the log N–log S at low fluxes. The results of this exercise are shown in Figure 16. From this figure, it is apparent that the log N–log S *must* break between $F_{100} \approx 2 \times 10^{-9}$ ph cm^2 s^{-1} and $F_{100} \approx 6.6 \times 10^{-8}$ ph cm^2 s^{-1}. For a small break (e.g., $\beta_1 - \beta_2 \approx 0.2$–0.3 and then $\beta_2 \approx 2.2$–2.3), the integrated emission of point sources would still match the intensity of the diffuse background at $F_{100} \approx 10^{-9}$ ph cm^2 s^{-1} which is sampled by *Fermi*. Thus, not only the break has to exist, but also this simple analysis shows that it has to be strong (see also Section 8.3), not to exceed the intensity of the diffuse emission.

The log N–log S in the whole band goes deeper than the source count distributions derived in the smaller bands. This is clearly shown in Figure 18. Given the fact that most of the source flux is emitted below 1 GeV (for reasonable photon indices), the source count distribution in the soft band (0.1–1.0 GeV) is the one which gets closer to the log N–log S in the whole band in terms of resolved diffuse flux.

The log N–log S in the whole bands shows a strong break with a faint-end slope (e.g., β_2) robustly constrained to be <2. In this case, the integral reported in Equation (12) converges for small fluxes, and it can be evaluated at zero flux to assess the maximum contribution of *Fermi*-like sources to the diffuse background. This turns out to be $2.39(\pm 0.48) \times 10^{-6}$ ph cm^{-2} s^{-1} sr^{-1} (1.26×10^{-6} ph cm^{-2} s^{-1} sr^{-1} systematic uncertainty) which represents 23($\pm$5)% (12% systematic uncertainty) of the *Fermi* diffuse background (Abdo et al. 2010d). This is a correct result as long as the log N–log S of point sources (i.e., blazars) does not become steeper at fluxes below the ones currently sampled by *Fermi*. A given source population normally exhibits a source count distribution with a single downward break (e.g., see the case of radio-quiet AGN in Cappelluti et al. 2007). This break is of cosmological origin since it coincides with the change of sign of the evolution of that population. As can be clearly seen in the redshift distribution in Abdo et al. (2010e), the epoch of maximum growth of blazars corresponds to redshift 1.5–2.0,

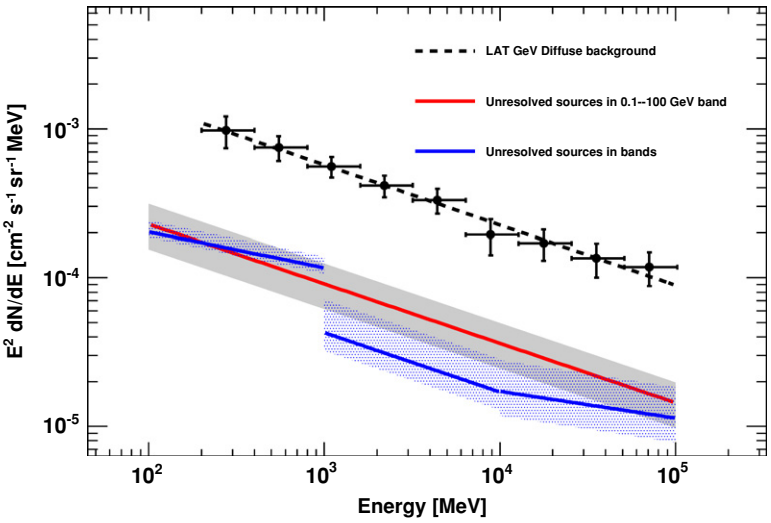

Figure 18. Contribution of point sources to the diffuse GeV background. The red solid line was derived from the study of the log N–log S in the whole band, while the blue solid lines come from the study of individual energy bands (see Section 7). The bands (gray solid and hatched blue) show the total (statistical plus systematic) uncertainty.

(A color version of this figure is available in the online journal.)

Table 6
Diffuse Emission Arising from Point Sources

Band (GeV)	EGB Intensity[a] (ph cm^{-2} s^{-1} sr^{-1})	Point Source Diffuse Emission (ph cm^{-2} s^{-1} sr^{-1})	Fraction of EGB Intensity (%)	$S_{\rm min}$[b] (ph cm^{-2} s^{-1})
0.1–100	1.03×10^{-5}	$1.63(\pm 0.18) \times 10^{-6}$	$15.8(\pm 1.8)$	9.36
0.1–1.0	9.89×10^{-6}	$1.54^{+0.29}_{-0.13} \times 10^{-6}$	$15.5^{+2.9}_{-1.3}$	51.1
1.0–10	3.85×10^{-7}	$2.93^{+1.95}_{-0.71} \times 10^{-8}$	$7.6^{+5.0}_{-1.8}$	3.58
10–100	1.50×10^{-8}	$1.36^{+0.84}_{-0.43} \times 10^{-9}$	$9.0^{+5.6}_{-2.8}$	0.61
0.1–100	1.03×10^{-5}	$2.39(\pm 0.48) \times 10^{-6}$	$22.5(\pm 1.8)$	0
0.1–1.0	9.89×10^{-6}	$2.07^{+0.98}_{-0.61} \times 10^{-6}$	$20.9^{+10.0}_{-6.1}$	0
1.0–10	3.85×10^{-7}	$5.49^{+4.36}_{-2.10} \times 10^{-8}$	$14.2^{+11.2}_{-5.4}$	0
10–100	1.50×10^{-8}	$>1.36 \times 10^{-6}$	>9.0	0[c]

Notes. The lower part of the table shows the values of the integrated emission when the source count distributions are extrapolated to zero flux. Errors are statistical only (see Section 5 for a discussion about systematic uncertainties).

[a] The intensities of the EGB emission are derived from Abdo et al. (2010d).

[b] Lower flux of integration of the source count distributions (see Equation (12)) in units of 10^{-10} ph cm^{-2} s^{-1}.

[c] The source count distribution in the 10–100 GeV does not show a break; and thus, its integral to zero flux diverges. As a lower limit on the diffuse emission, we adopted the value computed at the faintest detected source.

which coincides well with the peak of the star formation in the universe (e.g., Hopkins & Beacom 2006). Since *Fermi* is already sampling this population, it is reasonable to expect no other breaks in the source count distribution of blazars. Under this assumption, the result of the integration of Equation (12) is correct. The results of this exercise are shown in Figure 19 and summarized in Table 6. Since the 10–100 GeV source count distribution does not show a break, its integral diverges for small fluxes. Thus, in both Figure 19 and Table 6, we decided to adopt, as a lower limit to the contribution of sources to the diffuse emission in this band, the value of the integral evaluated at the flux of the faintest detected source.

The different levels of contribution to the diffuse background as a function of energy band might be the effect of the mixing of the two blazar populations. In other words, as shown in Section 7, FSRQs are the dominant population below 1 GeV, while BL Lac objects are the dominant one above 10 GeV. Given also that FSRQs are softer than BL Lac objects (see also Section 3), it is naturally to expect a modulation in the blazar contribution to the diffuse emission as a function of energy. This can clearly be seen in Figure 20, which shows the contribution of FSRQs and BL Lac objects to the diffuse emission. This has been computed integrating the source count distribution of Table 4 to the minimum detected source flux which is 9.36 $\times 10^{-10}$ ph cm^{-2} s^{-1} and 1.11 $\times 10^{-8}$ ph cm^{-2} s^{-1} for BL Lac objects and FSRQs, respectively. It is clear that FSRQs are contributing most of the blazar diffuse emission below 1 GeV while BL Lac objects, given their hard spectra, dominate above a few GeVs. The spectrum of the diffuse emission arising from the blazar class is thus curved, being soft at low energy (e.g., below 1 GeV) and hard at high energy (above 10 GeV), in agreement with the results of the analysis of the source count distributions in different bands.

8.1. Additional Tests

8.2. Source Count Distribution above 300 MeV

The effective area of the LAT quickly decreases below 300 MeV while at the same time both the PSF size and the intensity of the diffuse background increase (e.g., see Atwood

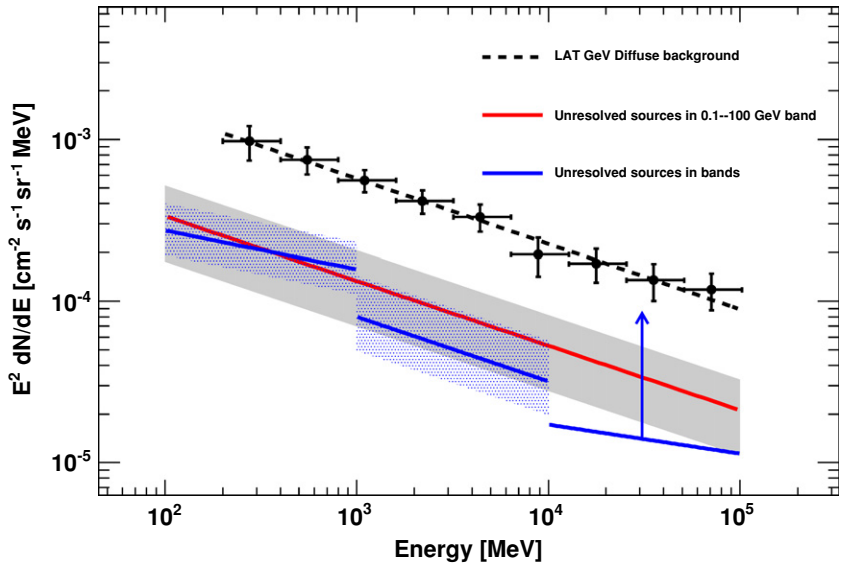

Figure 19. Contribution of point sources to the diffuse GeV background obtained by extrapolating and integrating the log N–log S to zero flux. The red solid line was derived from the study of the log N–log S in the whole band, while the blue solid lines come from the study of individual energy bands (see Section 7). The bands (gray solid and hatched blue) show the total (statistical plus systematic) uncertainty. The arrow indicates the lower limit on the integration of Equation (12) for the 10–100 GeV band.

(A color version of this figure is available in the online journal.)

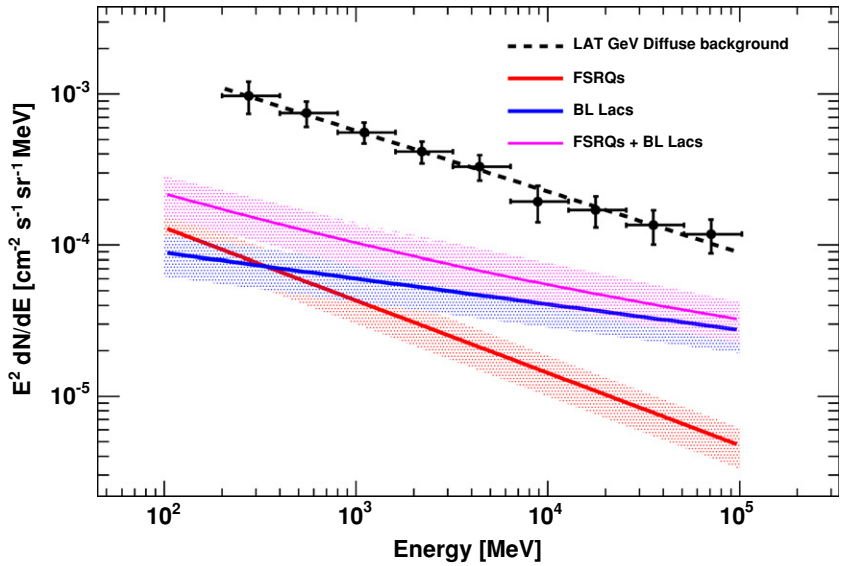

Figure 20. Contributions of different classes of blazars to the diffuse GeV background obtained by integrating the log N–log S. The red and the blue solid lines show the contribution of FSRQs and BL Lac objects, respectively, while the pink solid line shows the sum of the two. The bands around each line show the total (statistical plus systematic) uncertainty.

(A color version of this figure is available in the online journal.)

et al. 2009). In particular at the lowest energies, systematic uncertainties in the instrument response might compromise the result of the ML fit to a given source (or set of sources). In order to overcome this limitation, we constructed, with the method outlined in Section 7, the log N–log S of point sources in the 300 MeV–100 GeV band. Considering that in the $E > 100$ MeV band, the log N–log S shows a break around (6–7) $\times 10^{-8}$ ph cm^{-2} s^{-1}, and assuming a power law with a photon index of 2.4, we would expect to detect a break in the ($E \geqslant 300$ MeV) log N–log S around $\sim$1.5 $\times 10^{-8}$ ph cm^{-2} s^{-1}. Indeed, as shown in Figure 21, the break is detected at 1.68($\pm$0.33) $\times 10^{-8}$ ph cm^{-2} s^{-1}. Moreover, as Figure 21 shows, the break of the log N–log S and the one of the sky coverage are at different fluxes. More precisely, the source counts start to bend down before the sky coverage does it. This is an additional confirmation, along with the results of Section 7, that the break of the log N–log S is not caused by the sky coverage. The parameters of this additional source count distribution are reported for reference in Table 5.

8.3. Simulating a log N–log S without a Break

In order to rule out the hypothesis that the sources detected by *Fermi* produce most of the GeV diffuse emission, we performed an additional simulation. In this exercise, the input log N–log S is compatible with a single power law with a differential slope of 2.23. At bright fluxes, this log N–log S is compatible with the one reported in Abdo et al. (2009a) and at fluxes $F_{100} \geqslant 10^{-9}$ ph cm^{-2} s^{-1} accounts for $\sim$70% of

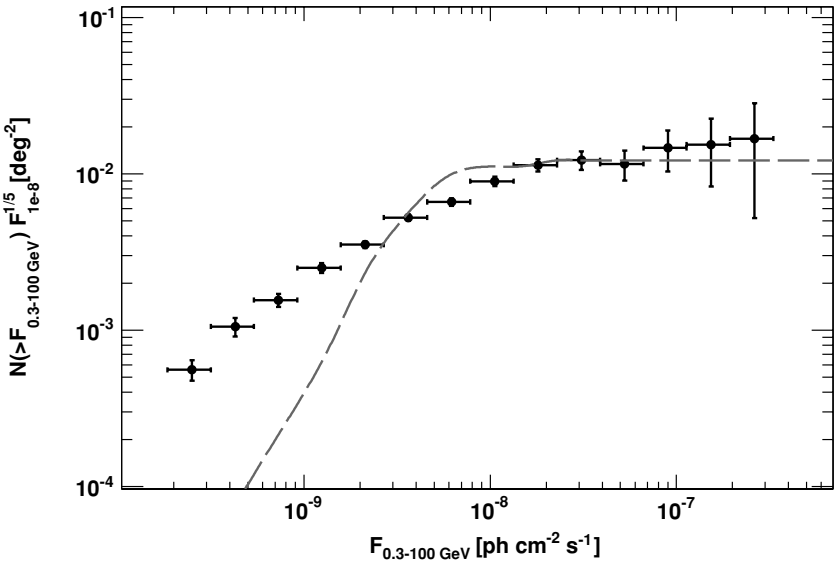

Figure 21. Source count distribution of all (TS $\geqslant$ 25 and $|b| \geqslant 10^{\circ}$) sources in the 300 MeV–100 GeV band. The distribution has been multiplied by $(F_{100}/10^{-8})^{1.5}$. The dashed line shows the sky coverage (scaled by an arbitrary factor) used to derive the source counts. Note that the break of the log N–log S and that one of the sky coverage are at different fluxes.

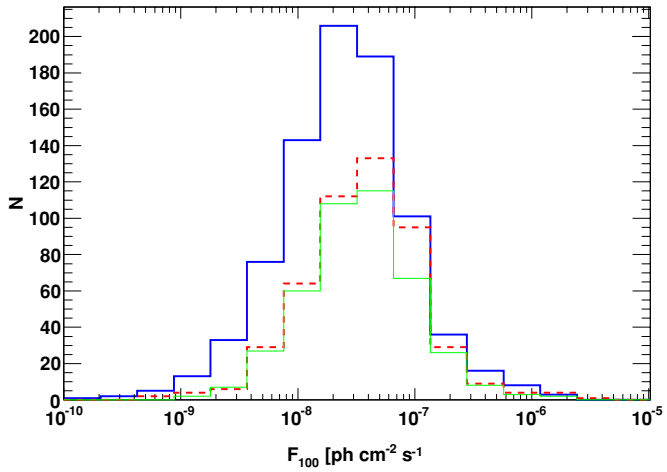

Figure 22. Flux distributions of detected sources (TS $\geqslant$ 50 and $|b| \geqslant 20^{\circ}$) for three different realizations of the γ-ray sky. The solid thick line corresponds to a log N–log S distribution which resolves ~70% of the GeV diffuse background, while the dashed line corresponds to the log N–log S derived in this work which resolves ~23% of the diffuse background. For comparison, the thin solid line shows the flux distributions of the real sample of sources detected by *Fermi*.

(A color version of this figure is available in the online journal.)

the EGB. In this scenario, the surface density of sources at $F_{100} \geqslant 10^{-9}$ ph cm^{-2} s^{-1} is 0.8 deg^{-2} (while the one we derived in Section 6.8 is 0.12 deg^{-2}). To this simulation, we applied the same analysis steps used for both the real data and the simulations analyzed in Section 4. Figure 22 compares the flux distribution of the sources detected in this simulation with the distribution of the real sources detected by LAT and also with the sources detected in one of the simulations used in Section 4. It is apparent that the flux distribution of the sources detected in the simulation under study here is very different from the other two.

Indeed, in the case where pointlike sources produce most of the EGB, *Fermi* should detect many more medium-bright sources than are actually seen. A K-S test yields that the probability that the flux distribution (arising from the log N–log S tested in this section) comes from the same parent population as the real data is $\leqslant 10^{-5}$. This probability becomes 5×10^{-4} if the χ^2-test is used. The K-S test between the flux distribution of one of the simulations used in Section 4 and the real data yields a probability of ~87% that both come from the same parent population while it is ~91% if the χ^2-test is used.

Thus, the hypothesis that *Fermi* is resolving (for $F_{100} \geqslant 10^{-9}$ ph cm^{-2} s^{-1}), the majority of the diffuse background can be ruled out at high confidence.

9. DISCUSSION AND CONCLUSIONS

Fermi provides a huge leap in sensitivity for the study of the γ-ray sky with respect its predecessor EGRET. This work focuses on the global intrinsic properties of the source population detected by *Fermi* at high Galactic latitudes.

We constructed the source count distribution of all sources detected above $|b| \geqslant 20^{\circ}$. This distribution extends over three decades in flux and is compatible at bright fluxes (e.g., $F_{100} \geqslant 6 \times 10^{-8}$ ph cm^{-2} s^{-1}) with a Euclidean function. Several methods have been employed to show that at fainter fluxes the log N–log S displays a significant flattening. We believe that this flattening has a cosmological origin and is due to the fact that *Fermi* is already sampling, with good accuracy, the part of the luminosity function that shows negative evolution (i.e., a decrease of the space density of sources with increasing redshift). This is the first time that such flattening has been found in the source count distributions of γ-ray sources and blazars. We also showed that the log N–log S of blazars closely follows that of point sources, showing that most of the unassociated high-latitude sources in the 1FLG catalog are likely to be blazars. At the fluxes currently sampled by *Fermi* (e.g., $F_{100} \geqslant 10^{-9}$ ph cm^{-2} s^{-1}), the surface density of blazars is $0.12^{+0.03}_{-0.02}$ deg^{-2} and this is found to be a factor ~4 larger than previous estimates.

The average intrinsic spectrum of blazars is in remarkably good agreement with the spectrum of the GeV diffuse emission recently measured by *Fermi* (Abdo et al. 2010d). Nevertheless, integrating the log N–log S, to the minimum detected source flux, shows that at least $16.0^{+2.4}_{-2.6}$% (the systematic uncertainty

is an additional 7%) of the GeV background can be accounted for by source populations measured by *Fermi*. This is a small fraction of the total intensity and it is bound not to increase dramatically unless the $\log N$–$\log S$ becomes steeper at fluxes below 10^{-9} ph cm^{-2} s^{-1}. This generally never happens unless a different source class starts to be detected in large numbers at fainter fluxes.

Thompson et al. (2007) predict the integrated emission of starburst galaxies to be 10^{-6} ph cm^{-2} s^{-1} sr^{-1} (above 100 MeV). This would represent ∼10% of the LAT diffuse background and would be comparable (although a bit less) to that of blazars found here. Indeed, their prediction that M82 and NGC 253 would be the first two starburst galaxies to be detected has been fulfilled (Abdo et al. 2010a). A similar contribution to the GeV diffuse background should arise from the integrated emission of normal star-forming galaxies (Pavlidou & Fields 2002). In both cases (normal and starburst galaxies), γ-rays are produced from the interaction of cosmic rays with the interstellar gas (e.g., see Abdo et al. 2009b). It is natural to expect that both normal and starburst galaxies produce a fraction of the diffuse emission since now both classes are certified γ-ray sources (see, e.g., Abdo et al. 2010b).

It is also interesting to note that pulsars represent the second largest population in our high-latitude sample (see Table 2). According to Faucher-Giguere & Loeb (2010), pulsars and, in particular, millisecond pulsars can produce a relevant fraction of the GeV diffuse emission. However, given the strong break, typically at a few GeVs, in their spectra (e.g., see Abdo et al. 2010f), millisecond pulsars are not expected to contribute much of the diffuse emission above a few GeVs. Finally, radio-quiet AGNs might also contribute to the GeV diffuse background. In these objects, the γ-ray emission is supposedly produced by non-thermal electrons present in the corona above the accretion disk (see, e.g., Inoue et al. 2008, for details). Inoue & Totani (2009) predict that, at fluxes of $F_{100} \leqslant 10^{-10}$ ph cm^{-2} s^{-1}, radio-quiet AGNs outnumber the blazars. According to their prediction, most of background could be explained in terms of AGNs (radio-quiet and radio-loud).

It is thus clear that standard astrophysical scenarios can be invoked to explain the GeV extragalactic diffuse background. However, the main result of this analysis is that blazars account only for <40% of it.[58] It remains a mystery why the average spectrum of blazars is so similar to the EGB spectrum. Taken by itself, this finding would lead one to believe that blazars might account for the entire GeV diffuse background. However, we showed (see Figure 22 and Section 8.3, for details) that in this case *Fermi* should have detected a much larger number (up to ∼50%) of medium-bright sources with a typical flux of $F_{100} \geqslant 10^{-8}$ ph cm^{-2} s^{-1}. This scenario can thus be excluded with confidence. Thus, the integrated emission from other source classes should still have a spectrum declining as a power law with an index of ∼2.4. This does not seem to be a difficult problem to overcome. Indeed, at least in the case of star-forming galaxies, we note that in the modeling of both Fields et al. (2010) and Makiya et al. (2010) the integrated emission from these sources displays a spectrum similar to the EGB one (at least for energies above 200 MeV). Moreover, in this work, we also found that the contribution to the diffuse emission of FSRQs and BL Lac objects is different, FSRQs being softer than BL Lac objects. Thus, the summed spectrum of their integrated diffuse emission is curved, softer at low energy and hard at high (> 10 GeV) energy. This makes it slightly different from the featureless power law of the diffuse background. All of the estimates presented here will be refined with the derivation of the blazar luminosity function, which is left to a follow-up paper.

[58] This includes extrapolating the source count distribution to zero flux and taking into account statistical and systematic uncertainties.

Helpful comments from the referee are acknowledged. The *Fermi* LAT Collaboration acknowledges generous ongoing support from a number of agencies and institutes that have supported both the development and the operation of the LAT as well as scientific data analysis. These include the National Aeronautics and Space Administration and the Department of Energy in the United States; the Commissariat à l'Energie Atomique and the Centre National de la Recherche Scientifique/Institut National de Physique Nucléaire et de Physique des Particules in France; the Agenzia Spaziale Italiana and the Istituto Nazionale di Fisica Nucleare in Italy; the Ministry of Education, Culture, Sports, Science and Technology (MEXT), High Energy Accelerator Research Organization (KEK), and Japan Aerospace Exploration Agency (JAXA) in Japan; and the K. A. Wallenberg Foundation, the Swedish Research Council, and the Swedish National Space Board in Sweden. Additional support for science analysis during the operations phase is gratefully acknowledged from the Istituto Nazionale di Astrofisica in Italy and the Centre National d'Études Spatiales in France.

Facility: Fermi

REFERENCES

Abdo, A. A., et al. 2009a, ApJ, 700, 597
Abdo, A. A., et al. 2009b, ApJ, 703, 1249
Abdo, A. A., et al. 2010a, ApJ, 709, L152
Abdo, A. A., et al. 2010b, ApJS, 188, 405
Abdo, A. A., et al. 2010c, ApJ, 710, 1271
Abdo, A. A., et al. 2010d, Phys. Rev. Lett., 104, 101101
Abdo, A. A., et al. 2010e, ApJ, 715, 429
Abdo, A. A., et al. 2010f, ApJ, 713, 154
Ahn, E., Bertone, G., Merritt, D., & Zhang, P. 2007, Phys. Rev. D, 76, 023517
Ajello, M., Greiner, J., Kanbach, G., Rau, A., Strong, A. W., & Kennea, J. A. 2008, ApJ, 678, 102
Ajello, M., et al. 2009, ApJ, 699, 603
Atwood, W. B., et al. 2009, ApJ, 697, 1071
Avni, Y. 1976, ApJ, 210, 642
Bergström, L. 2000, Rep. Prog. Phys., 63, 793
Berrington, R. C., & Dermer, C. D. 2003, ApJ, 594, 709
Burnett, T. H., Kerr, M., & Roth, M. 2009, arXiv:0912.3855
Cappelluti, N., et al. 2007, ApJS, 172, 341
Chiang, J., & Mukherjee, R. 1998, ApJ, 496, 752
Ciprini, S., et al. 2007, in AIP Conf. Ser. 921, The First GLAST Symposium, ed. S. Ritz, P. Michelson, & C. A. Meegan (Melville, NY: AIP), 546
D'Agostini, G. 1995, Nucl. Instrum. Methods Phys. Res. A, 362, 487
Dermer, C. D. 2007, ApJ, 659, 958
Eddington, A. S., Sir 1940, MNRAS, 100, 354
Faucher-Giguere, C., & Loeb, A. 2010, J. Cosmol. Astropart. Phys., JCAP01(2010)05
Fichtel, C. E., Hartman, R. C., Kniffen, D. A., Thompson, D. J., Ogelman, H., Ozel, M. E., Tumer, T., & Bignami, G. F. 1975, ApJ, 198, 163
Fields, B. D., Pavlidou, V., & Prodanovic, T. 2010, arXiv:1003.3647
Gabici, S., & Blasi, P. 2003, Astropart. Phys., 19, 679
Hartman, R. C., et al. 1999, ApJS, 123, 79
Hasinger, G., Burg, R., Giacconi, R., Hartner, G., Schmidt, M., Trumper, J., & Zamorani, G. 1993, A&A, 275, 1
Hopkins, A. M., & Beacom, J. F. 2006, ApJ, 651, 142
Inoue, Y., & Totani, T. 2009, ApJ, 702, 523
Inoue, Y., Totani, T., & Ueda, Y. 2008, ApJ, 672, L5
Jungman, G., Kamionkowski, M., & Griest, K. 1996, Phys. Rep., 267, 195
Keshet, U., Waxman, E., Loeb, A., Springel, V., & Hernquist, L. 2003, ApJ, 585, 128
Loeb, A., & Waxman, E. 2000, Nature, 405, 156
Makiya, R., Totani, T., & Kobayashi, M. A. R. 2010, arXiv:1005.1390

Marcha, M. J. M., Browne, I. W. A., Impey, C. D., & Smith, P. S. 1996, MNRAS, 281, 425
Miniati, F. 2002, MNRAS, 337, 199
Mücke, A., & Pohl, M. 2000, MNRAS, 312, 177
Narumoto, T., & Totani, T. 2006, ApJ, 643, 81
Pavlidou, V., & Fields, B. D. 2002, ApJ, 575, L5
Pfrommer, C., Enßlin, T. A., & Springel, V. 2008, MNRAS, 385, 1211
Reimer, O., & Thompson, D. J. 2001, Proc. 27th ICRC, 6, 2566
Sreekumar, P., et al. 1998, ApJ, 494, 523
Stecker, F. W., & Salamon, M. H. 1996, ApJ, 464, 600
Stocke, J. T., Morris, S. L., Gioia, I. M., Maccacaro, T., Schild, R., Wolter, A., Fleming, T. A., & Henry, J. P. 1991, ApJS, 76, 813
Strong, A. W., Moskalenko, I. V., & Reimer, O. 2004, ApJ, 613, 956
Thompson, T. A., Quataert, E., & Waxman, E. 2007, ApJ, 654, 219
Ullio, P., Bergström, L., Edsjö, J., & Lacey, C. 2002, Phys. Rev. D, 66, 123502
Urry, C. M., & Padovani, P. 1995, PASP, 107, 803
Wilks, S. S. 1938, Ann. Math. Stat., 9, 60